nature cell biology

A ROR1–HER3–lncRNA signalling axis modulates the Hippo–YAP pathway to regulate bone metastasis

Chunlai Li[1,13], Shouyu Wang[1,13,14], Zhen Xing[1], Aifu Lin[1,14], Ke Liang[1], Jian Song[2], Qingsong Hu[1], Jun Yao[1], Zhongyuan Chen[3,4], Peter K. Park[1], David H. Hawke[5], Jianwei Zhou[6], Yan Zhou[7], Shuxing Zhang[8], Han Liang[3,5], Mien-Chie Hung[1,9,10], Gary E. Gallick[2], Leng Han[11], Chunru Lin[1,9,15] and Liuqing Yang[1,9,12,15]

Bone metastases remain a serious health concern because of limited therapeutic options. Here, we report that crosstalk between ROR1–HER3 and the Hippo–YAP pathway promotes breast cancer bone metastasis in a long noncoding RNA-dependent fashion. Mechanistically, the orphan receptor tyrosine kinase ROR1 phosphorylates HER3 at a previously unidentified site Tyr1307, following neuregulin stimulation, independently of other ErbB family members. p-HER3 Tyr1307 recruits the LLGL2–*MAYA*–NSUN6 RNA–protein complex to methylate Hippo/MST1 at Lys59. This methylation leads to MST1 inactivation and activation of YAP target genes in tumour cells, which elicits osteoclast differentiation and bone metastasis. Furthermore, increased ROR1, p-HER3 Tyr1307 and *MAYA* levels correlate with tumour metastasis and unfavourable outcomes. Our data provide insights into the mechanistic regulation and linkage of the ROR1–HER3 and Hippo–YAP pathway in a cancer-specific context, and also imply valuable therapeutic targets for bone metastasis and possible therapy-resistant tumours.

Bone metastasis continues to be a severe health concern although significant progress has been made. When bone metastatic lesions develop, bone residential tumour cells produce a cohort of osteolytic factors[1]. These osteolytic factors, including connective tissue growth factor (CTGF), trigger differentiation of osteoclast precursors derived from monocytes[2]. *CTGF* is one of the signature genes that are significantly upregulated in patients with relapse to the bone compared with patients with relapse elsewhere according to gene expression analysis[3].

The Hippo–YAP pathway controls cell proliferation, tumorigenesis, chemoresistance and metastasis in human tumours[4–6]. The core Hippo cassette comprises an MST1/2 (Hippo), LATS1/2 (large tumour suppressor kinase1/2), and YAP (yes-associated protein) signalling cascade[7,8]. MST1/2 is a protein serine/threonine kinase that negatively regulates cell growth, and mutation of the Hippo genes leads to organ overgrowth[9,10]. In mammals, MST1/2 phosphorylates LATS1/2, which further phosphorylates YAP for cytoplasmic sequestration and degradation[11]. When MST1/2 kinase activity is inhibited, by an unknown mechanism, YAP accumulates in the nucleus for transcriptional activation[12].

The receptor tyrosine kinase (RTK)-like orphan receptors (RORs), like all other RTKs[13], possess an extracellular ligand-binding domain, yet their ligands, cellular effects, and downstream signalling pathways are largely unknown[14]. The two ROR family members, ROR1 and ROR2, were originally found to be involved in skeletal, cardiorespiratory and neurological development[15,16]. Increasing evidence has indicated that both ROR proteins are highly expressed in multiple human cancer types, including leukaemia, ovarian cancer and breast cancer[17–22]. Although ROR1 was treated as a pseudokinase originally, on the basis of the observation that ROR1 was unable to be autophosphorylated[23,24], some studies have also demonstrated

[1]Department of Molecular and Cellular Oncology, The University of Texas MD Anderson Cancer Center, Houston, Texas 77030, USA. [2]Department of Genitourinary Medical Oncology, The University of Texas MD Anderson Cancer Center, Houston, Texas 77030, USA. [3]Department of Bioinformatics and Computational Biology, The University of Texas MD Anderson Cancer Center, Houston, Texas 77030, USA. [4]Department of Statistics, Rice University, Houston, Texas 77030, USA. [5]Department of Systems Biology, The University of Texas MD Anderson Cancer Center, Houston, Texas 77030, USA. [6]Department of Molecular Cell Biology and Toxicology, School of Public Health, Nanjing Medical University, 140 Hanzhong Road, Nanjing 210029, China. [7]Department of Oncology, Yixing People's Hospital, 75 Zhenguan Road, Yixing 214200, China. [8]Department of Experimental Therapeutics, The University of Texas MD Anderson Cancer Center, Houston, Texas 77030, USA. [9]The Graduate School of Biomedical Sciences, The University of Texas MD Anderson Cancer Center, Houston, Texas 77030, USA. [10]Center for Molecular Medicine and Graduate Institute of Cancer Biology, China Medical University, Taichung 404, Taiwan. [11]Department of Biochemistry and Molecular Biology, The University of Texas Health Science Center at Houston McGovern Medical School, Houston, Texas 77030, USA. [12]Center for RNA Interference and Non-Coding RNAs, The University of Texas MD Anderson Cancer Center, Houston, Texas 77030, USA. [13]These authors contributed equally to this work. [14]Present addresses: Department of Molecular Cell Biology and Toxicology, School of Public Health, Nanjing Medical University, 140 Hanzhong Road, Nanjing 210029, China (S.W.); College of Life Sciences, Zhejiang University, Hangzhou 310058, China (A.L.).
[15]Correspondence should be addressed to C.L. or L.Y. (e-mail: clin2@mdanderson.org or lyang7@mdanderson.org)

Received 30 June 2016; accepted 15 December 2016; published online 23 January 2017; DOI: 10.1038/ncb3464

the moderate autocatalytic kinase activity of ROR1 *in vitro*[25–27]. The mechanisms of the enzymatic activity, substrates and downstream signalling pathway of ROR1 are still elusive.

Cytoplasmic long noncoding RNAs (lncRNAs) are involved in regulating messenger RNA stabilization and transport as well as microRNA sponging[28–31]. It has also been suggested that cytoplasmic lncRNAs are important mediators of intracellular signalling pathways. For example, *lnc-DC* modulates the phosphorylation status of STAT3[32], *NKILA* regulates IkB phosphorylation and degradation[33], and *LINK-A* regulates HIF1α signalling[34].

Here, we demonstrate that neuregulin-1 (NRG1) triggers the heterodimerization of ROR1 and HER3, leading to HER3 phosphorylation by ROR1 at Tyr1307. Phosphorylated HER3 recruits the adaptor protein LLGL2, lncRNA *MAYA* (MST1/2-antagonizing for YAP activation), and methyltransferase NSUN6, which methylates MST1 at Lys59. The methylation abolishes MST1 kinase activity and activates YAP and target genes. These events lead to cancer cell-induced osteoclast differentiation and bone resorption. Our studies identify the crosstalk between the ROR1/HER3–LLGL2–*MAYA*–NSUN6 signalling axis and the Hippo–YAP pathway, and suggest a promising therapeutic strategy for bone metastatic patients.

RESULTS

ROR1 promotes the colonization and growth of breast cancer cells within the bone

Enhanced ROR1 level has been observed in many blood and solid malignancies. To access its function and regulation under a tumour-specific context, we first surveyed the genetic alterations of the *ROR1* gene. In sarcoma, ovarian, pancreatic, breast and lung cancer types, the *ROR1* locus is amplified in 2–6% of patients (Fig. 1a). In breast cancer, the *ROR1* locus is amplified in the triple-negative breast cancer (TNBC) subtype compared with the status of other biomarkers (Supplementary Fig. 1a). ROR1 expression is significantly upregulated in TNBC compared with non-TNBC subtypes (Fig. 1b and Supplementary Fig. 1b). Immunohistochemical (IHC) staining of breast cancer tissue microarrays (TMAs) revealed that high levels of ROR1 correlated with the TNBC subtype and poor survival (Fig. 1c,d and Supplementary Table 1). Furthermore, ROR1 expression is more correlated with non-small cell lung carcinoma (NSCLC) than with small cell lung carcinoma (Supplementary Fig. 1c). To enable functional characterization of ROR1, we generated ROR1 knockout (KO) breast cancer cell lines using CRISPR–Cas9 technology (Supplementary Fig. 1d,e). Two individual clones of the ROR1 KO breast cancer cell line exhibited reduced proliferation (Supplementary Fig. 1f,g). ROR1 KO also inhibited migration and invasion of breast cancer cells, and overexpression of wild-type (WT) ROR1, but not the kinase-dead K506A mutant[27], rescued the migration and invasion of ROR1 KO cells (Supplementary Fig. 1h–k).

It has recently been reported that ROR1 mediates alternative Wnt signalling to activate the YAP pathway for organ development[35], which prompts us to examine the expression of YAP1-regulated genes[36–39] in ROR1 KO cells. Significantly, the expression of 37 out of the 57 YAP1-regulated genes was downregulated by depletion of ROR1 (Fig. 1e). Activation of YAP has been shown to promote tumour progression and metastasis[40,41]. Furthermore, YAP1-regulated genes including *CTGF* may play important roles in promoting osteolysis during bone metastatic lesion development[42]. Consistently, we found hyper-activation of the YAP pathway and elevated expression of CTGF in bone metastatic BoM-1833 cells[3] compared with parental MDA-MB-231 cells. Interestingly, the ROR1 protein level is upregulated in BoM-1833 cells, and ROR1 KO reduced CTGF production (Fig. 1f,g). Then we determined the role of ROR1 in cancer cell-induced osteoclast differentiation. We found that the differentiation of osteoclast precursors to mature osteoclasts was stimulated with conditioned media (CM) from parental but not ROR1 KO BoM-1833 cells, and this impaired osteoclast differentiation was rescued by CM from ROR1 KO cells expressing WT ROR1 but not K506A mutant (Fig. 1h,i). Interestingly, CM from ROR1 KO BoM-1833 cells supplemented with recombinant CTGF rescued osteoclast differentiation (Supplementary Fig. 1l and Fig. 1j).

Next, we aimed to determine the role of ROR1 in breast cancer bone metastasis. BoM-1833 cells, containing a stably expressed firefly luciferase reporter, were inoculated to nude mice via intracardiac injection, and metastatic progression was monitored weekly by bioluminescence imaging (BLI). The tumour burden of mouse limbs was greatly reduced by ROR1 KO (Fig. 1k,l). The bone metastatic lesion number was also decreased when ROR1 was knocked out (Fig. 1m). Therefore, these data suggest the important role of ROR1 in promoting the colonization and growth of breast cancer cells within the bone through regulation of the Hippo–YAP pathway.

ROR1 phosphorylates HER3 at Tyr1307 in an ErbB-independent manner

To identify the potential substrates or regulators of ROR1, we immunoprecipitated endogenous ROR1 and identified ROR1-binding proteins by mass spectrometry (MS). Interestingly, we found that HER3 was the top protein that binds ROR1 (Supplementary Fig. 2a and Supplementary Table 2). The ROR1-associated HER3 harboured a previously unknown phosphorylation site of Tyr1307 (Fig. 2a and Supplementary Table 2). Hence, we generated phosphorylation-specific antibodies targeting p-HER3 (Tyr1307) (Supplementary Fig. 2b) for further cellular and tissue studies.

It has been well established that HER3 forms heterodimers with EGFR and HER2 in response to NRG1 and plays important roles in a variety of cancer types[43,44]. We hypothesized that ROR1 and HER3 might form heterodimers, and found that HER3 associated with EGFR, HER4 and ROR1 following NRG1 stimulation (Fig. 2b). NRG1 triggered the phosphorylation at previously known HER3 tyrosine sites (Tyr1197, Tyr1222, Tyr1289 and Tyr1328)[45] as well as at a previously unknown Tyr1307 site (Fig. 2c). Although the pan-EGFR inhibitor dacomitinib (PF299804) abolished HER3 phosphorylation at those four tyrosine sites, neither tyrosine phosphorylation of Tyr1307 nor the ROR1–HER3 interaction was affected by this inhibitor (Fig. 2d). In contrast, ROR1 knockdown abolished phosphorylation of HER3 at Tyr1307 but not at the EGFR-dependent phosphorylation sites (Fig. 2e).

Next, we found that knockdown of EGFR showed minimal effects on the ROR1–HER3 interaction or the status of p-HER3 (Tyr1307) (Fig. 2f). NRG1 stimulation triggered interaction between exogenous ROR1 and HER3, as well as p-HER3 (Tyr1307) in ERBB-null 32D cells (Fig. 2g), suggesting a possibility that ROR1 may directly phosphorylate HER3. *In vitro* kinase assay showed that full-length

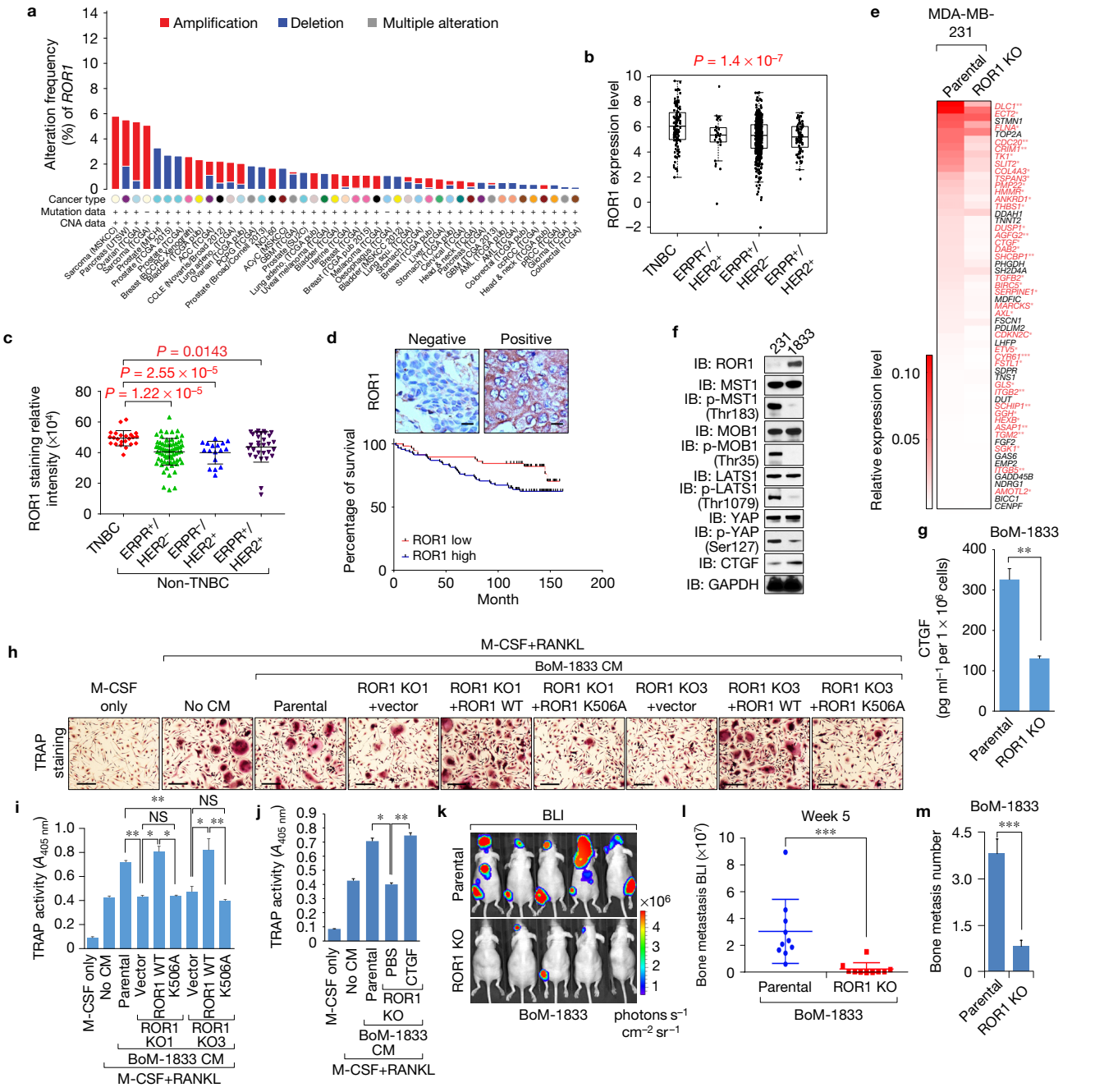

Figure 1 ROR1 promotes the colonization and growth of breast cancer cells within the bone. (**a**) Distribution of alteration frequency of *ROR1* in multiple cancer types. Details in parentheses indicate the source of the corresponding tumour dataset and the year of publication. CNA, copy-number alteration. (**b**) Box plot comparing ROR1 expression in TNBC, ERPR$^-$/HER2$^+$, ERPR$^+$/HER2$^-$ and ERPR$^+$/HER2$^+$ breast cancer subtypes ($n = 119$, 30, 482, 80 tumours respectively, one-way ANOVA). The boxes show the median ± 1 quartile, with whiskers extending to the most extreme data point within 1.5 interquartile ranges from the box boundaries. (**c**) IHC detection of ROR1 in TNBC, ERPR$^-$/HER2$^+$, ERPR$^+$/HER2$^-$ and ERPR$^+$/HER2$^+$ breast cancer subtypes ($n = 23$, 72, 17 and 30 tumours respectively; median ±1 quartile, one-way ANOVA). (**d**) Survival analysis of ROR1 -low and -high breast cancer patients (top, scale bars, 40 μm; bottom, $n = 58$ and 92 patients respectively, log rank test). (**e**) Heatmap representing colour-coded expression levels of 57 YAP1 target genes in parental and ROR1 KO cells. (**f**) Immunoblotting (IB) detection of the indicated proteins in MDA-MB-231 or BoM-1833 cells. (**g**) CTGF ELISA assay in parental and ROR1 KO BoM-1833 cells. (**h**,**i**) Osteoclast differentiation assays in the presence of M-CSF only, M-CSF+RANKL, combined M-CSF+RANKL and conditioned media (CM) from ROR1 KO BoM-1833 cells or KO cells transfected with the indicated plasmids (**h**, scale bars, 200 μm; **i**, quantification). *A*, absorbance. (**j**) Quantification of osteoclast differentiation in the presence of M-CSF only, M-CSF+RANKL, combined M-CSF+RANKL and CM from ROR1 KO BoM-1833 cells or CM from ROR1 KO BoM-1833 cells KO supplemented with PBS or recombinant CTGF (50 ng ml^{-1}). (**k**–**m**) Representative BLI images (**k**), BLI signal quantification (**l**, $n = 10$ mice per group) and metastatic tumour numbers (**m**) of mice intracardially injected with parental or ROR1 KO BoM-1833 cells at week 5. For **e**,**g**,**i**,**j**,**l** and **m**, mean ± s.e.m. were derived from $n = 3$ independent experiments (NS (not significant), $P > 0.05$; $^*P < 0.05$; $^{**}P < 0.01$; $^{***}P < 0.001$; two-tailed paired Student's *t*-test). Unprocessed original scans of all blots with size markers for **f** are shown in Supplementary Fig. 9. Statistics source data for **d**,**h**,**i**,**k** and **l** are in Supplementary Table 8.

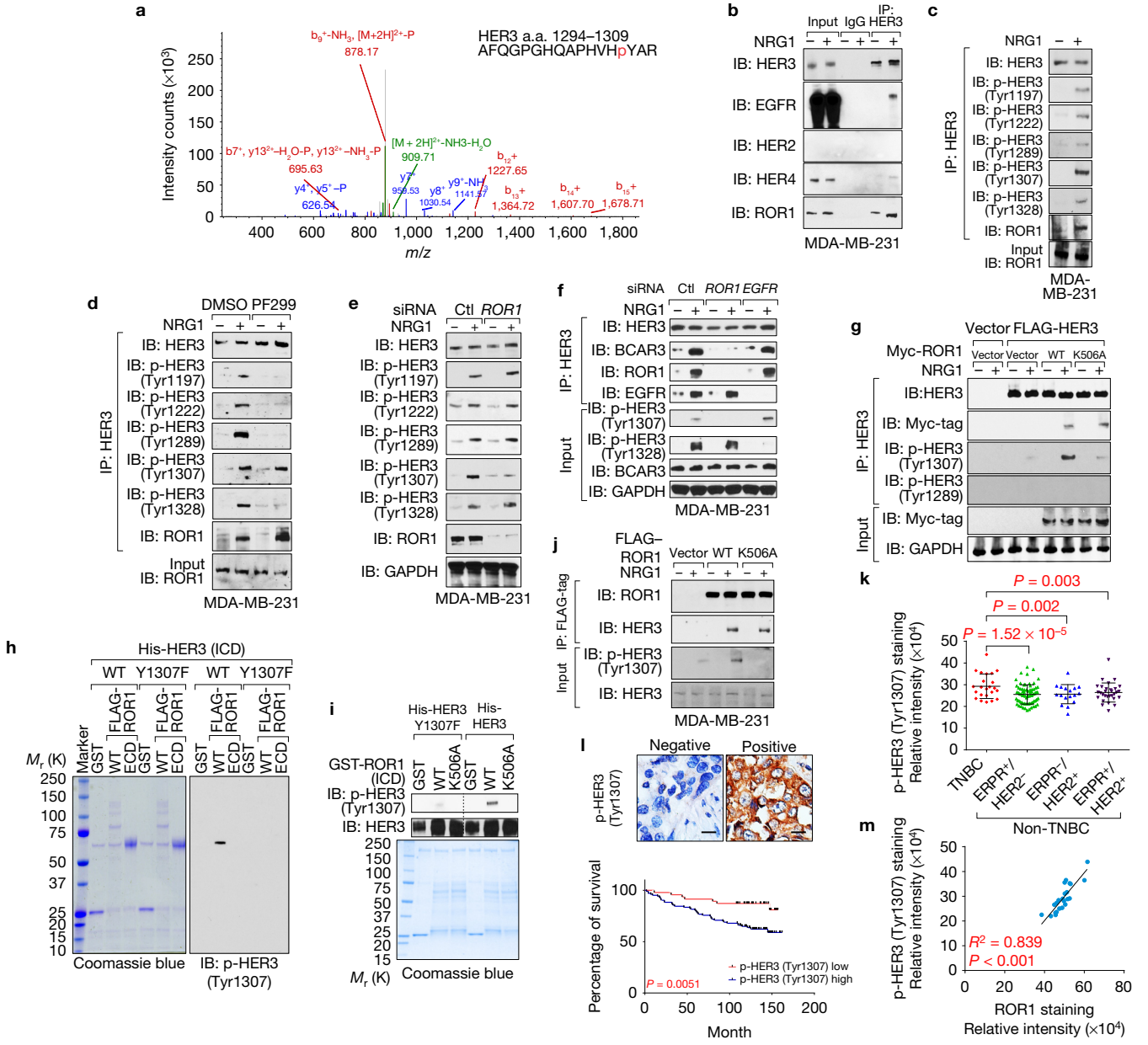

Figure 2 ROR1-dependent phosphorylation of HER3 at Tyr1307 correlates with breast cancer clinical parameters. (**a**) Annotated MS/MS spectrum assigned to the HER3 peptide AFQGPGHQAPHVH[p]YAR, at 926.924 Da. Data acquired from analysis of the tryptic digest by high-sensitivity LC-MS/MS on an Orbitrap Elite high-resolution mass spectrometer. (**b**) Immunoprecipitation (IP) and IB detection of the indicated proteins in MDA-MB-231 cells with NRG1 treatment. (**c**,**d**) IP followed by IB detection of HER3 phosphorylation and HER3–ROR1 interaction in MDA-MB-231 cells without transfection (**c**), and pre-treated with dacomitinib (PF299, 100 nM) (**d**) followed by NRG1 treatment. (**e**) IB detection of the indicated proteins in cells transfected with the indicated siRNAs followed by NRG1 treatment. (**f**,**g**) IP and IB detection of the indicated proteins in MDA-MB-231 cells transfected with the indicated siRNAs (**f**) or 32D cells transfected with the indicated expression vectors (**g**) followed by NRG1 stimulation. (**h**,**i**) *In vitro* kinase assay was performed using His_6-HER3 intracellular domain (ICD) WT or Y1307F mutant and FLAG-tagged ROR1 WT or extracellular domain (ECD) (**h**) or His_6-FL HER3, GST-tagged WT ROR1 ICD or K506A mutant (**i**). (**j**) IP and IB detection of the indicated proteins in MDA-MB-231 cells transfected with the indicated plasmids followed by NRG1 treatment. (**k**) IHC staining intensity of p-HER3 (Tyr1307) in TNBC, ERPR-/HER2+, ERPR+/HER2- and ERPR+/HER2+ breast cancer subtypes ($n = 23$, 72, 17 and 30 patients respectively, median ±1 quartile, one-way ANOVA). (**l**) Kaplan–Meier survival analysis of p-HER3 (Tyr1307)-low and -high breast cancer patients by IHC staining (top, scale bars, 40 μm; bottom, $n = 43$ and 107 patients respectively, log rank test). (**m**) Correlation analysis showing the positive correlation of staining intensity of ROR1 (Fig. 1c) with that of p-HER3 (Tyr1307) within the TNBC subgroup. Fisher's exact test was used ($n = 23$ patients, $P < 0.001$; R^2, correlation coefficient). Unprocessed original scans of all blots with size markers are shown in Supplementary Fig. 9. Statistics source data for **l** are in Supplementary Table 8.

(FL) ROR1 but not the extracellular domain (ECD) phosphorylated the HER3 intracellular domain (ICD) at the Tyr1307 site (Fig. 2h). Consistently, bacterially expressed ICD of WT ROR1, but not K506A mutant, phosphorylates HER3 at Tyr1307 *in vitro* (Fig. 2i). In breast cancer cells, expression of ROR1 K506A mutant abolished Tyr1307 phosphorylation of HER3 following NRG1 stimulation (Fig. 2j).

It has been reported that ROR1 is tyrosine phosphorylated by c-MET and SRC at the proline-rich domain and the kinase domain, respectively[46]. Our data indicated that neither the tyrosine phosphorylation of ROR1 nor the ROR1-SRC/MET interaction was affected by NRG1 stimulation (Supplementary Fig. 2c). Although ROR1 tyrosine phosphorylation was abolished by an SRC inhibitor, saracatinib, the NRG1-induced p-HER3 (Tyr1307) was not significantly affected (Supplementary Fig. 2d). In 32D cells, ROR1 exhibited undetectable tyrosine phosphorylation and association with SRC (Supplementary Fig. 2e), suggesting that the NRG1-triggered ROR1–HER3 pathway is independent of EGFR–SRC–MET signalling in breast cancer cells.

High levels of HER3 expression correlate with unfavourable outcomes for TNBC patients[47,48]. To ascertain whether p-HER3 (Tyr1307) promotes proliferation and invasion of breast cancer cells, we knocked out HER3 and found that HER3 KO impaired cell proliferation and mobility (Supplementary Fig. 2f–k). p-HER3 (Tyr1307) is highly increased in TNBC compared with other breast cancer subtypes (Fig. 2k). Further, the p-HER3 (Tyr1307) correlates with breast cancer patient outcomes (Fig. 2l). Interestingly, the level of ROR1 in TNBC strongly correlates with p-HER3 Tyr1307 status ($R^2 = 0.839$) (Fig. 2m). Furthermore, the p-HER3 (Tyr1307) is elevated in lung adenocarcinomas compared with normal lung tissues (Supplementary Fig. 2l); lung adenocarcinomas at the metastatic stage (TnN>0M≥0) showed an increased p-HER3 (Tyr1307) level compared with the non-metastatic stage (TnN0M0) (Supplementary Fig. 2l). A high level of p-HER3 (Tyr1307) also correlates with unfavourable outcomes for lung adenocarcinoma patients (Supplementary Fig. 2m).

Crosstalk between ROR1–HER3 and Hippo–YAP pathway

Phosphorylation of a receptor tyrosine kinase triggers the recruitment of proteins that contain an SH2 domain to mediate downstream signalling[49]. The SH2-domain-containing protein BCAR3 (breast cancer anti-oestrogen resistance 3) identified by MS (see Supplementary Fig. 2a) could be recruited to p-HER3 (Tyr1307). To test this, we mutated HER3 Tyr1307 to phenylalanine (Y1307F) and Tyr1197/Tyr1222/Tyr1289/Tyr1328 to phenylalanine (4Y-F). We found that the expression of the HER3 Y1307F mutant, but not the 4Y-F mutant, abolished the HER3–BCAR3 interaction following NRG1 stimulation (Fig. 3a). Consistently, the deletion of the SH2 domain of BCAR3 abolished the HER3–BCAR3 interaction but showed no effect on p-HER3 (Tyr1307) (Fig. 3b). Next, we synthesized biotinylated-HER3 peptides harbouring either phosphorylated or unphosphorylated Tyr1197, Tyr1222, Tyr1289, Tyr1328 and Tyr1307 residues with their corresponding flanking amino acid sequences. Streptavidin pulldown showed that the HER3 peptide harbouring p-Tyr1307, but not other p-Tyr residues, strongly interacts with BCAR3 (Fig. 3c).

We further investigated the downstream signalling pathways of BCAR3. Recombinant protein pulldown assay indicated that BCAR3 directly binds LLGL2 (lethal giant larvae homologue 2) but not other proteins identified by MS (Fig. 3d). In *Drosophila*, the adaptor protein LLGL2 plays a critical role in mediating the Hippo–YAP pathway regulated by cell–cell junctions[50]. Our MS confirmed the associations of ROR1, HER3 and BCAR3 with LLGL2 (Supplementary Fig. 3a). Furthermore, a panel of Hippo complex proteins (STK4 (MST1), SAV1, MOB1 and RASSF1 (Ras association domain family member 1)) were observed to bind both ROR1 and LLGL2 (Supplementary Fig. 3a and Supplementary Table 3). MS also revealed the LLGL2 phosphorylation at Tyr499; thus, a site-specific antibody against p-LLGL2 (Tyr499) was generated (Supplementary Fig. 3b,c). ROR1 was the most plausible candidate for LLGL2 (Tyr499) phosphorylation in the context of this specific signalling cascade, and *in vitro* kinase assay confirmed this hypothesis (Fig. 3e). Consistently, overexpression of the kinase-dead mutant of ROR1 abolished phosphorylation of LLGL2 at Tyr499 in NRG1-treated cells (Supplementary Fig. 3d). Knockdown of BCAR3 eliminated the interaction between HER3 and LLGL2 as well as p-LLGL2 (Tyr499) (Fig. 3f). GST-LLGL2 pulldown showed that both non-phosphorylated (No-P-) and phosphorylated (P-) LLGL2 bind BCAR3, but only P-LLGL2 (Tyr499) binds MST1 (Fig. 3g).

A previously unknown dimethylation modification of MST1 at Lys59 (MST1 (Lys59me2)) was also identified from MS and confirmed by methylation-specific antibodies (Supplementary Fig. 3e and Supplementary Table 3 and Supplementary Fig. 3f). Lysophosphatidic acid (LPA) has been shown to trigger YAP1 activation via G-protein-coupled receptor signalling[51]. Our data showed that NRG1, but not LPA, triggered MST1 (Lys59me2), and MST1 methylation status negatively correlates with MST1 (Thr183) phosphorylation and YAP1 (Ser127) phosphorylation (Fig. 3h and Supplementary Fig. 3g).

LncRNA *MAYA* is involved in YAP activation

We found a putative protein methyltransferase, NSUN6, in both ROR1 and LLGL2 pulldown experiments (see Supplementary Fig. 2a and 3a). NSUN6 is an RNA-binding ribosomal protein that can mediate RNA methylation[52]. Therefore, we hypothesized that lncRNA molecules could associate with NSUN6 to regulate MST1 methylation. To identify the lncRNAs that might be involved in the YAP signalling pathway, we transfected the human Lincode siRNA library into MCF-7 cells that were engineered with a TEAD-driven luciferase reporter, and subsequently the relative YAP1 activity was determined. We set up a threshold at $\log_2 \leq -3$ (red line) to pinpoint 40 lncRNAs that were potentially required for YAP1-dependent transcription (Fig. 4a and Supplementary Table 4).

We then picked up the top five lncRNAs for RNA pulldown experiments to identify whether they bind the Hippo–YAP pathway proteins. Interestingly, *LOC645249* (*MNX1-AS1*) binds LLGL2, MST1, SAV1, MOB1, NSUN6 and RASSF1, suggesting that it may mediate the YAP pathway activation; thus, we renamed this lncRNA as MST1/2-antagonizing lncRNA for YAP activation (*MAYA*) (Supplementary Fig. 4a and Supplementary Table 5). We performed a 5′- and 3′- rapid amplification of cDNA ends (RACE) assay to determine the entire sequence of *MAYA*, confirming that the sequence detected in MDA-MB-231 cells is identical to that archived in the RefSeq database (Supplementary Fig. 4b). The expression pattern and splicing variation of *MAYA* in human tissues and breast cancer cells were validated by northern blot (Supplementary Fig. 4c,d).

The Cancer Genome Atlas (TCGA) database mining revealed that *MAYA* expression is upregulated in breast cancer compared with normal tissue in both matched and unmatched sample pools (Fig. 4b). In addition, RNAscope analysis confirmed that 71% and 62% of breast cancer tissues exhibited positive *MAYA* staining in training and validation studies respectively (Fig. 4c). Furthermore, *MAYA* expression in breast cancer is associated with advanced

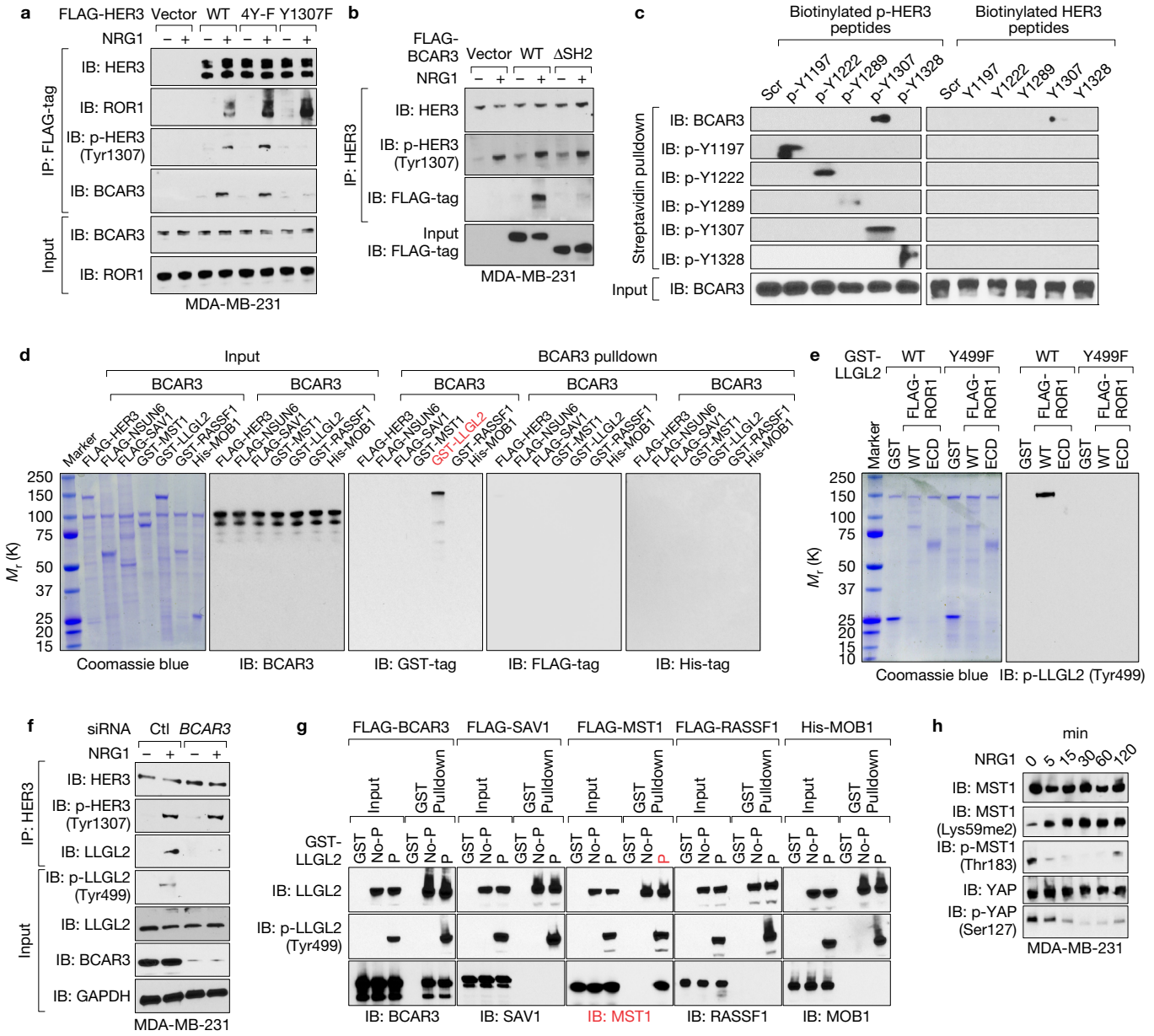

Figure 3 Crosstalk between ROR1–HER3 and the Hippo–YAP pathway. (**a**) IP followed by IB detection of ROR1–HER3 interaction, p-HER3 (Tyr1307) phosphorylation, and p-HER3–BCAR3 interaction in MDA-MB-231 cells transfected with the indicated plasmids followed by NRG1 treatment. (**b**) IP followed by IB detection of the indicated proteins in MDA-MB-231 cells transfected with the indicated plasmids followed by NRG1 treatment. (**c**) Peptide pulldown assay using phosphorylated or unphosphorylated peptides harbouring the indicated amino acids with the corresponding flanking sequence were subjected to IB detection using the indicated antibodies. (**d**) *In vitro* pulldown assay was performed by incubating BCAR3 with the indicated recombinant proteins. BCAR3-associated proteins were detected by IB using the indicated antibodies. (**e**) *In vitro* phosphorylation assay was performed using FLAG-tagged WT ROR1 or extracellular domain (ECD) and GST-tagged LLGL2. (**f**) IP and IB detection of the indicated proteins in cells transfected with the indicated siRNAs followed by NRG1 stimulation. (**g**) GST pulldown assay was performed by incubating either unphosphorylated (No-P)- or Tyr499 phosphorylated (P)-LLGL2 with the indicated recombinant proteins. The associated proteins were detected by IB using the indicated antibodies. Positive interactions are shown in red. (**h**) IB detection of the indicated proteins in MDA-MB-231 cells treated with NRG1 according to the indicated time course. Unprocessed original scans of all blots with size markers are shown in Supplementary Fig. 9.

stage (TnN>0M≥0) ($P = 0.049$) (Fig. 4d) and unfavourable patient outcomes ($P = 0.0085$) (Fig. 4e). As revealed by RNAscope 2.0 analysis, *MAYA* was upregulated in the majority of human solid tumours (Supplementary Fig. 4e). High levels of *MAYA* also correlate with lung adenocarcinoma, metastatic stage (TnN>0M≥0) and poor outcomes (Supplementary Fig. 4f,g).

We next tested whether *MAYA* is required for YAP1 activation in this specific signalling context, finding that *MAYA* depletion significantly impaired the occupancy of YAP1 on the promoter of its target genes (Fig. 4f) and expression of these genes under NRG1 stimulation (Fig. 4g,h). The phosphorylations of MST1 (Thr183), MOB1 (Thr35), LATS1 (Thr1079) and YAP (Ser127) were all

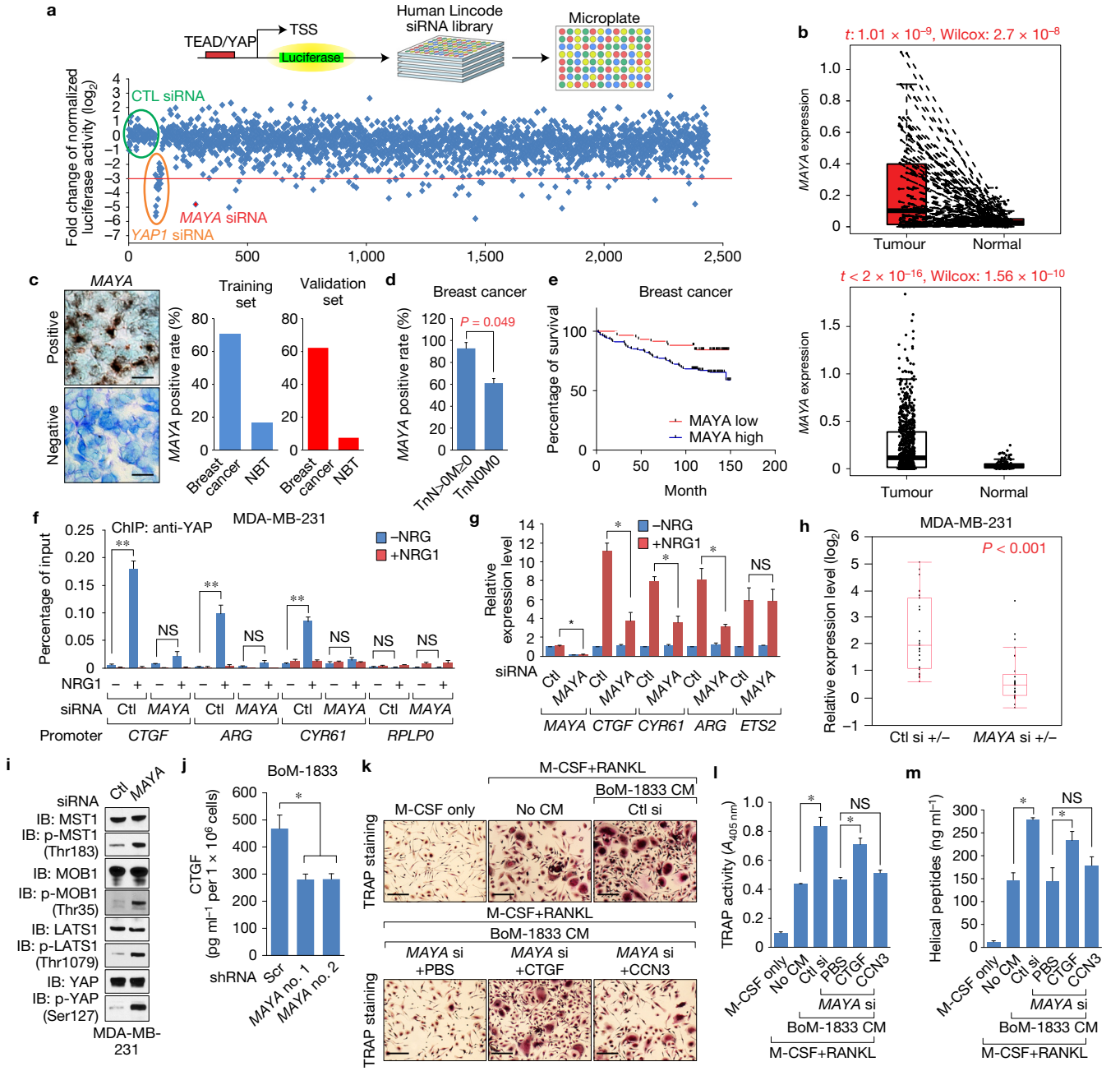

Figure 4 LncRNA *MAYA* is required for activation of YAP. (**a**) Screening of the human Lincode siRNA library in MCF-7 cells. The red line defines the threshold of eightfold change in luciferase activity (*MAYA* siRNA versus CTL siRNA). TSS, transcription start site. (**b**) Box plots comparing *MAYA* expression in matched (top) and unmatched (bottom) breast tumours and normal tissues (top, $n=105$ patients for each group; bottom, $n=837$ and 105 patients respectively, Wilcoxon test). (**c**) *MAYA* expression in breast tumour or normal tissue (NBT). Left, RNAScope, scale bars, 40 μm; right, quantification of training ($n=54$ tumours and 60 NBTs) and validation ($n=180$ tumours and 30 NBTs) sets based on two independent experiments. (**d**) *MAYA* expression in non-metastatic (TnN0M0) and metastatic (TnN>0M≥0) breast tumours ($n=38$ and 62 tumours respectively). (**e**) Kaplan–Meier survival analysis of *MAYA*-low and -high breast cancer patients ($n=57$ and 103 patients respectively, log rank test). (**f**) ChIP-qPCR detection of YAP1 occupancy on the promoter of YAP1 target genes in NRG1-treated cells. (**g**) RT-qPCR detection of the indicated genes in cells transfected with the indicated siRNAs followed by NRG1 treatment. (**h**) Box plot comparing the expression level of 29 YAP1 target genes in MDA-MB-231 cells transfected with the indicated siRNAs (mean ± s.e.m. were derived from $n=3$ independent experiments, $P<0.001$, Wilcoxon test). (**i**) IB detection of the indicated proteins in *MAYA* knockdown MDA-MB-231 cells. (**j**) Quantification of CTGF in BoM-1833 cells harbouring the indicated shRNAs. (**k**,**l**) TRAP staining (**k**, scale bars, 200 μm) and quantification (**l**) of osteoclast differentiation following treatment with M-CSF, M-CSF+RANKL or combined M-CSF+RANKL and CM from the indicated siRNA-transfected BoM-1833 cells supplemented with CTGF (50 ng ml^{-1}) or CCN3 (50 ng ml^{-1}). (**m**) Measurement of helical peptides released from human bone plates incubated with primary osteoclasts treated as in **k**. For **b** and **h**, the boxes show the median ± 1 quartile, with whiskers extending to the most extreme data point within 1.5 interquartile ranges from the box boundaries. For **d**,**f**,**g**,**j**,**l** and **m**, mean ± s.e.m. were derived from $n=3$ independent experiments (NS (not significant), $P>0.05$; $^{*}P<0.05$; $^{**}P<0.01$; two-tailed paired Student's *t*-test). Unprocessed original scans of all blots with size markers are shown in Supplementary Fig. 9. Statistics source data for **c** and **k**–**l** are in Supplementary Table 8.

increased following *MAYA* knockdown (Fig. 4i). Accordingly, *MAYA* knockdown significantly reduced CTGF secretion in BoM-1833 cells (Fig. 4j), and consequently impaired cancer cell-induced osteoclast differentiation and bone resorption, which could be partially rescued by introduction of recombinant CTGF (Fig. 4k–m). Notably, *MAYA* is not involved in LPA or cell-density-dependent YAP1-target-gene regulation (Supplementary Fig. 4h,i).

LncRNA-mediated, NSUN6-dependent methylation inhibits the kinase activity of MST1

RNA pulldown in cell lysates showed that only the sense transcript of *MAYA* binds a panel of Hippo pathway proteins (Supplementary Fig. 5a,b). However, *in vitro* RNA pulldown with bacterially expressed recombinant proteins revealed that only LLGL2 and NSUN6 directly bind *MAYA* (Fig. 5a), and the interactions were further confirmed by RNA immunoprecipitation (RIP) assay (Fig. 5b). LLGL2 contains 14 WD40 repeats that act as scaffolds to interact with RNA molecules for cellular functions[50,53]. To map the RNA-binding region of LLGL2, we generated a series of LLGL2 deletion mutants, finding that removal of the first three WD40 domains (ΔWD^{1-3}) of LLGL2 (Δ36–169) abolished the *MAYA*–LLGL2 interaction (Fig. 5c). Similarly, the PUA domain of NSUN6 (Δ111–203) is required for the *MAYA*–NSUN6 interaction (Fig. 5d). The necessity of the WD40 domains 1–3 of LLGL2 and the PUA domain of NSUN6 for *MAYA* binding was confirmed *in vivo* by RIP assay (Fig. 5e).

To characterize the specific RNA sequences required for these interactions, we performed an *in vitro* RNA pulldown followed by a dot-blot assay as previously described[34,53]. We found that sequence B1 (nucleotides 241–300) of *MAYA* is essential for LLGL2 binding, and D3 (nucleotides 841–900) is responsible for NSUN6 binding (Fig. 5f), which was further confirmed by RNA pulldown assay with the corresponding *MAYA* mutants (Supplementary Fig. 5c and Fig. 5g). Furthermore, RNA electrophoretic mobility shift assay indicated that the sequences of nucleotides 251–290 and nucleotides 851–890 of *MAYA* directly bind LLGL2 and NSUN6, respectively (Supplementary Fig. 5d). Both RNA fluorescence *in situ* hybridization (FISH) and cell fractionation assay indicated that *MAYA* is localized to the cytosol (Fig. 5h and Supplementary Fig. 5e). Immuno-RNA FISH and RIP assays suggested that *MAYA* co-localized with LLGL2 following NRG1 stimulation, which was impaired in the presence of the LLGL2 Y499F mutant (Fig. 5h,i).

In the presence of FL *MAYA*, but not the ΔLLGL2 or ΔNSUN6 deletion transcripts, bacterially expressed LLGL2 could pulldown NSUN6 *in vitro* (Fig. 6a). These experiments suggested that the LLGL2–*MAYA*–NSUN6 complex might be responsible for MST1 methylation on Lys59. To test this, we performed an *in vitro* protein methylation assay and observed that only NSUN6 was able to methylate MST1 in the presence of SAM (*S*-adenosyl methionine) (Fig. 6b). Lys59 of MST1, in charge of ATP-binding, is critical for the kinase activity and autophosphorylation of MST1[54]. We found that mutation of MST1 Lys59 to alanine or knockdown of NSUN6 impaired NRG1-triggered MST1 methylation at Lys59 (Fig. 6c,d). Consistently, knockout of LLGL2 or knockdown of *MAYA* abolished the methylation of MST1, leading to hyperphosphorylation of MST1 at Thr183 (Fig. 6e,f).

We further investigated the regulatory roles of LLGL2 and NSUN6 in modulating MST1 methylation. We found that both the LLGL2 Y499F and ΔWD^{1-3} deletion mutants abolished ligand-induced MST1 methylation (Fig. 6g). In addition, unphosphorylated LLGL2 (Y499F) still associated with NSUN6, but failed to recruit MST1 (Fig. 6g) while the ΔWD^{1-3} LLGL2 mutant could recruit MST1, but failed to associate with NSUN6 (Fig. 6g). Similarly, expression of both the NSUN6 ΔSAM (Δ242–248) and the ΔPUA (Δ111–203) mutants impaired MST1 methylation *in vivo* (Fig. 6h). To validate the hypothesis that methylation at Lys59 abolishes the kinase activity and autophosphorylation of MST1, we performed an *in vitro* methylation followed by a kinase assay. In the presence of SAM, methylated MST1 failed to be phosphorylated at Thr183, but the unmethylated MST1 was autophosphorylated at Thr183 in the presence of ATP (Fig. 6i). At the cellular level, LLGL2 KO but not NSUN6 KO, decreased cell proliferation (Supplementary Fig. 6a–d). However, both LLGL2 and NSUN6 KO reduced cell mobility (Supplementary Fig. 6e–h). Among 57 YAP1-regulated genes examined, NRG1-induced expression of 25, 37, 40 and 29 genes was significantly downregulated by ROR1 KO, LLGL2 KO, NSUN6 KO and HER3 KO, respectively, and 21 genes were commonly reduced (Fig. 6j). Thus, we have identified the crosstalk between the ROR1/HER3–LLGL2–*MAYA*–NSUN6 signalling axis and the Hippo pathway.

To further demonstrate the mechanistic linkage, we expressed WT ROR1 and the K506A mutant in ROR1 KO cells for rescue experiments. We found that the expression of WT ROR1, but not the K506A mutant, restored the NRG1-triggered phenotypes (Fig. 7a). Furthermore, we performed rescue experiments using HER3 Y1307E and LLGL2 Y499E phosphorylation-mimic mutants, respectively. The HER3 Y1307E mutant mediated the HER3–BCAR3 interaction and recruitment of LLGL2 to phosphorylated HER3 (Fig. 7b and Supplementary Fig. 7a), and expression of the LLGL2 Y499E mutant in ROR1 KO cells rescued MST1 methylation and YAP1 hypophosphorylation (Supplementary Fig. 7a and Fig. 7c), and activation of YAP1 target genes in the absence of NRG1 (Fig. 7d and Supplementary Fig. 7b,c).

Next, we knocked down *MAYA* by the locked nucleic acid (LNA) method and rescued the expression of *MAYA* using LNA-resistant FL *MAYA* or ΔLLGL2 and ΔNSUN6 mutants, respectively (Supplementary Fig. 7d,e). *MAYA* knockdown in both breast and lung cancer cells showed dramatic effects on NRG1-dependent MST1 (Lys59) methylation, but minimal effects on phosphorylations of HER3 (Tyr1307) and LLGL2 (Tyr499) (Fig. 7e and Supplementary Fig. 7f). The NRG1-induced expression of YAP1-regulated genes was attenuated in *MAYA* knockdown cells but rescued by expressing FL *MAYA*, but not ΔLLGL2 and ΔNSUN6 deletion mutants in these cells (Fig. 7f and Supplementary Fig. 7g,h). As a control, an NRG1-induced gene, *ETS2*[55], was not affected by *MAYA* knockdown (Supplementary Fig. 7i). Furthermore, CM from *MAYA* knockdown cells failed to enhance osteoclast differentiation (Fig. 7g and Supplementary Fig. 7j) and bone resorption by osteoclasts (Fig. 7h). Notably, these effects were rescued by CM from *MAYA* knockdown cells expressing FL *MAYA*, but not the ΔLLGL2 and ΔNSUN6 deletion mutants (Fig. 7g,h and Supplementary Fig. 7j).

MAYA serves as a promising therapeutic target for bone metastasis

We examined the expression level of *MAYA* in MDA-MB-231 parental and organ-specific metastatic derivatives, including LM2

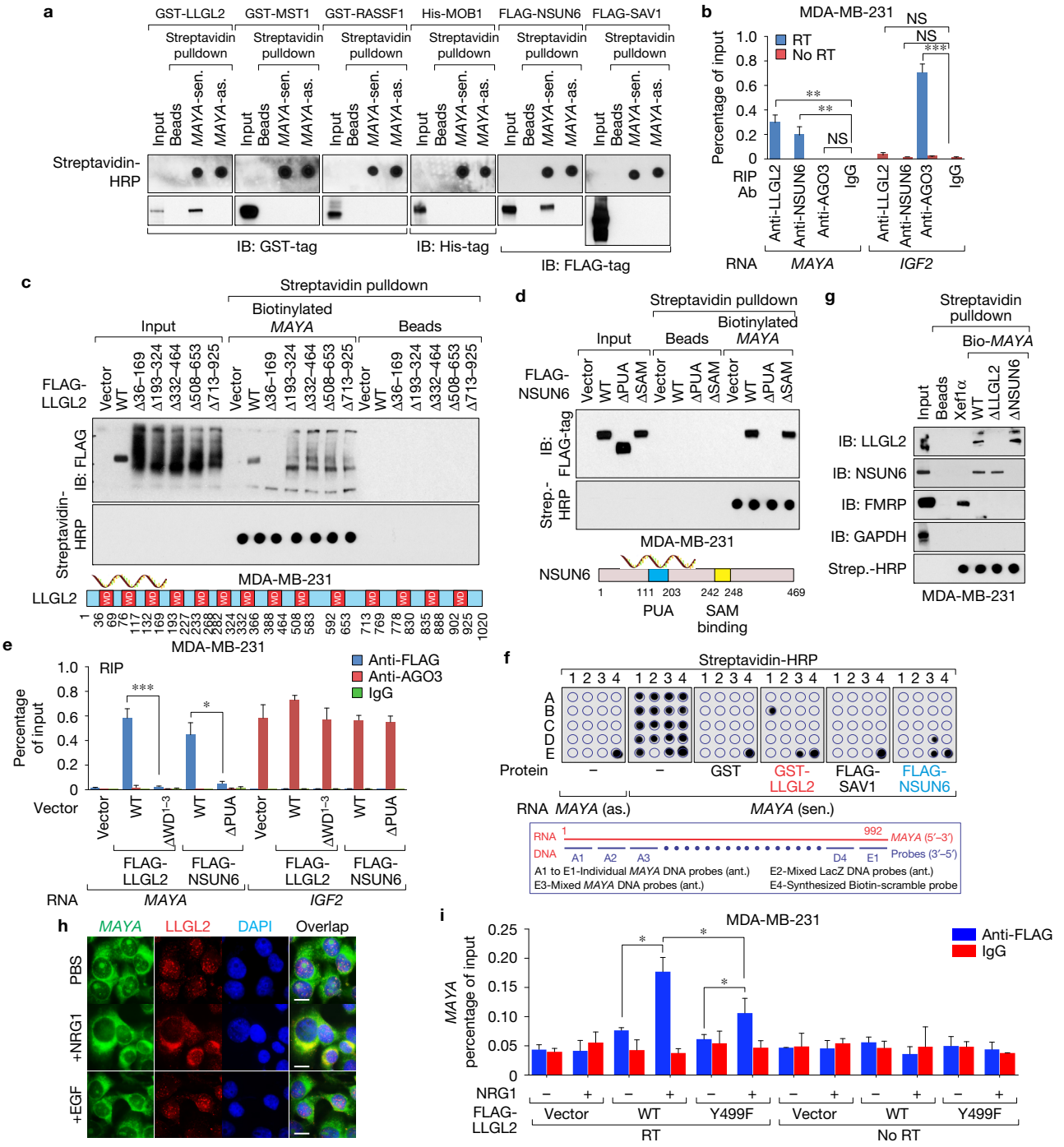

Figure 5 Characterization of *MAYA*–LLGL2–NSUN6 associations. (**a**) *In vitro* transcribed *MAYA* sense (sen.) or antisense (as.) transcripts were incubated with the indicated recombinant proteins for *in vitro* streptavidin RNA pulldown assay, followed by IB detection using the indicated antibodies. (**b**) RNA immunoprecipitation (RIP) assays were performed using the indicated antibodies in MDA-MB-231 cells. RT, reverse transcription. (**c**,**d**) Top panel: FLAG-tagged WT or deletion mutants of LLGL2 (**c**) and NSUN6 (**d**) expressed in MDA-MB-231 cells were subjected to streptavidin RNA pulldown assay with biotinylated *MAYA*, followed by IB using anti-FLAG antibody. The presence of RNA transcripts was detected using streptavidin-HRP by dot-blot assay. (**e**) RIP assay using the indicated antibodies in MDA-MB-231 cells transfected with the indicated plasmids. (**f**) *In vitro* RNA–protein binding followed by dot-blot assays using biotinylated *MAYA* sense (sen.) or antisense (as.) transcripts with recombinant proteins as indicated. Bottom, annotation of DNA probes targeting *MAYA* applied on the blot. (**g**) Streptavidin pulldown assay was performed using biotinylated FL, truncated *MAYA*, and *Xef1α* transcript and cell lysates extracted from MDA-MB-231 cells followed by IB using the indicated antibodies. The presence of RNA transcripts was detected using streptavidin-HRP by dot-blot assay. (**h**) Immuno-RNA FISH detection using FISH probes targeting *MAYA* and antibody targeting LLGL2 in MDA-MB-231 cells with the indicated treatment (scale bars, 20 μm). (**i**) RIP assay using anti-FLAG antibody in MDA-MB-231 cells transfected with the indicated plasmids followed by NRG1 treatment. For **b**,**e** and **i**, mean ± s.e.m. were derived from $n=3$ independent experiments (NS (not significant), $P>0.05$; $^{*}P<0.05$; $^{**}P<0.01$; $^{***}P<0.001$; two-tailed paired Student's *t*-test). Unprocessed original scans of all IB blots with size markers are shown in Supplementary Fig. 9. For **a**,**c**,**d**,**f** and **g**, unprocessed original scans of dot blots are also shown in Supplementary Fig. 9. Raw images of three independent experiments for **h** are in Supplementary Table 8.

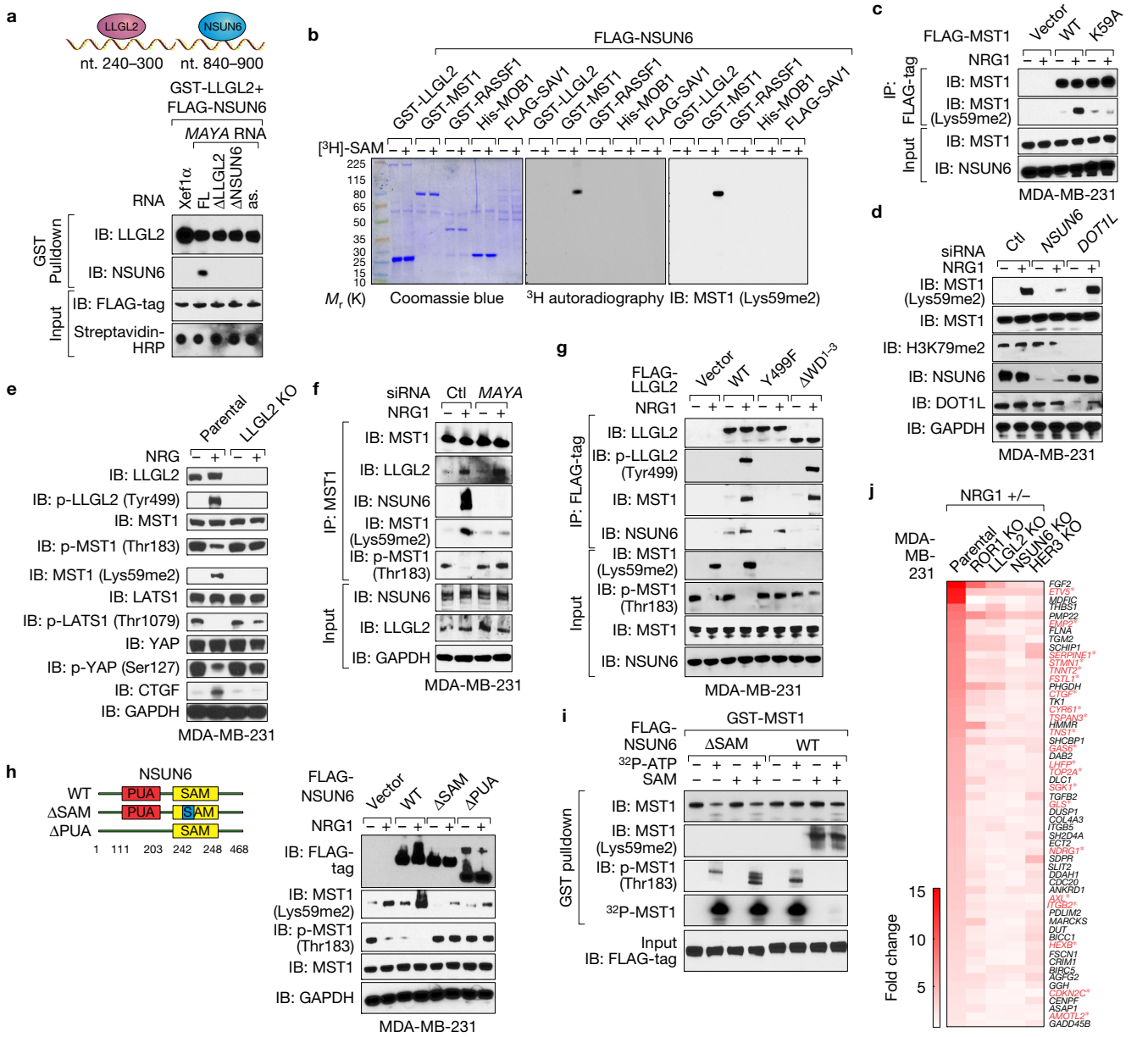

Figure 6 LncRNA-mediated, NSUN6-dependent methylation inhibits the kinase activity of MST1. (**a**) Top, schematic diagram showing the direct interactions of *MAYA* with LLGL2 and NSUN6. nt., nucleotides. Bottom, GST pulldown assay was performed by incubating GST-LLGL2 with NSUN6 in the presence of FL or domain deletion *MAYA* transcripts. LLGL2–NSUN6 interaction was detected by IB. (**b**) *In vitro* methylation assay was performed using recombinant FLAG-NSUN6 and the indicated recombinant proteins with or without [^{3}H]-SAM followed by autoradiography or IB detection with the indicated antibody. (**c**–**e**) IB detection of MST1 Lys59 methylation in MDA-MB-231 cells transfected with the indicated plasmids (**c**), siRNAs (**d**) or in LLGL2 KO cells (**e**) followed by NRG1 treatment. (**f**) IP and IB detection of the indicated proteins in MDA-MB-231 cells transfected with the indicated siRNAs followed by NRG1 treatment. (**g**) IP followed by IB detection of p-LLGL2 (Tyr499)- and NSUN6-dependent MST1 Lys59 methylation in MDA-MB-231 cells transfected with the indicated plasmids followed by NRG1 treatment. (**h**) Left, graphic illustration of NSUN6 domain deletion mutants; right, IB detection of MST1 Lys59 methylation and Thr183 phosphorylation in cells transfected with the indicated plasmids followed by NRG1 treatment. (**i**) *In vitro* methylation assay followed by kinase assay using GST-MST1 and FLAG-NSUN6 (WT and ΔSAM mutant) in the presence of [^{32}P]ATP and/or SAM. MST1 was purified by GST pulldown and detected by autoradiography or IB. (**j**) Heatmap representing colour-coded fold change of NRG1-induced 57 YAP1 target genes determined by RT-qPCR in parental, ROR1 KO, LLGL2 KO, NSUN6 KO and HER3 KO MDA-MB-231 cells. Twenty-one genes were found to be commonly downregulated under all of the KO conditions ($n = 3$ independent experiments, $^*P < 0.05$, two-tailed paired Student's *t*-test). Unprocessed original scans of all blots with size markers are shown in Supplementary Fig. 9.

(lung)[56], BoM-1833 (bone)[56], BRN (brain)[57], and a brain metastatic cell line derived from BT474 and its parental line[58]. We found that *MAYA* was highly expressed in BoM-1833 cells, suggesting the potential role of *MAYA* in bone metastasis from breast cancer (Supplementary Fig. 8a). In BoM-1833 cells, *MAYA* knockdown showed minimal effects on NRG1-dependent p-HER3 (Tyr1307) and p-LLGL2 (Tyr499), but dramatic effects on MST1 (Lys59me2) and NRG1-triggered hypophosphorylation of MST1, LATS1, YAP1, as

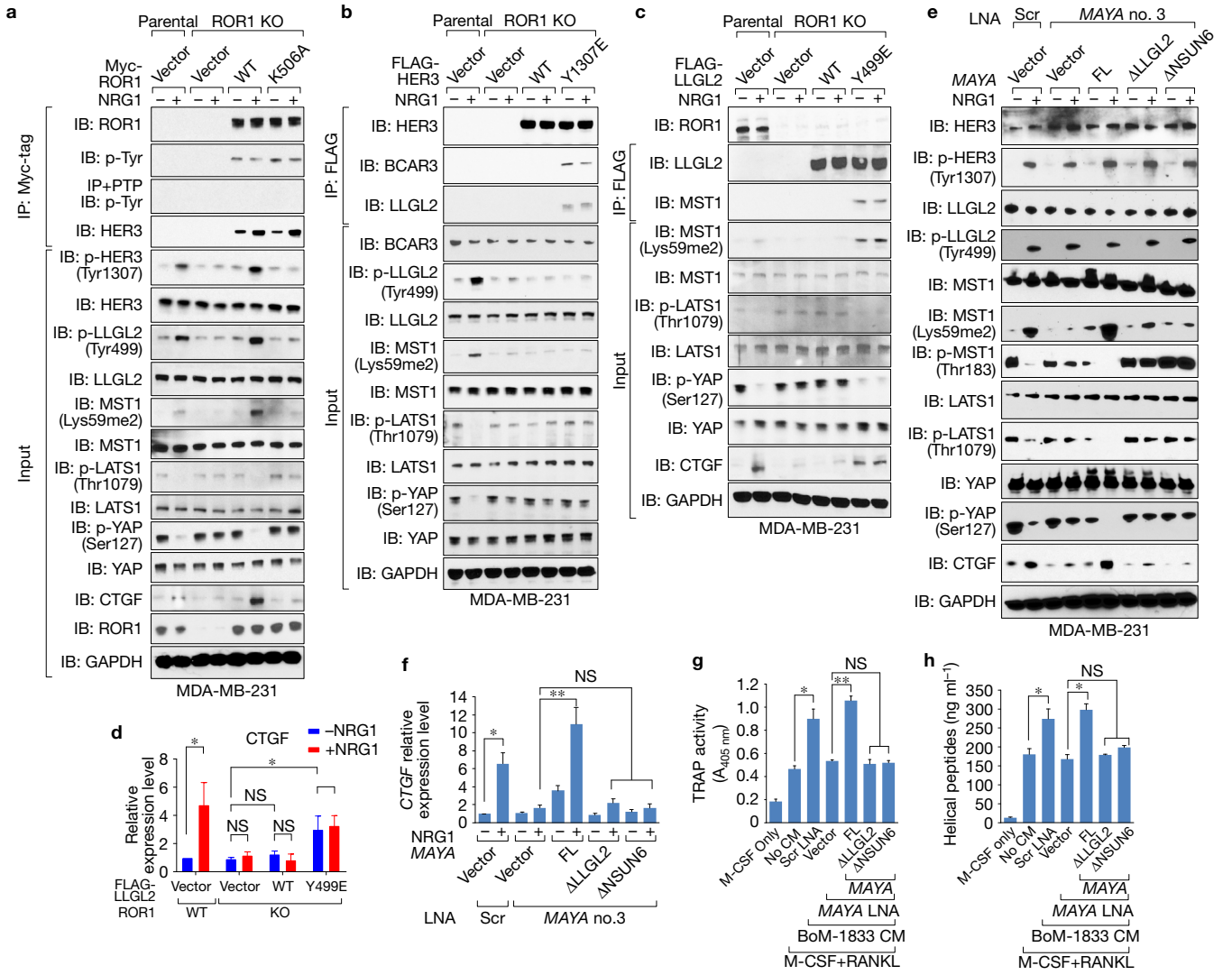

Figure 7 The ROR1/HER3–LLGL2/*MAYA*/NSUN6 signalling axis regulates YAP activity. (**a**–**c**) IP and IB detection of the indicated proteins in ROR1 KO cells transfected with the indicated plasmids followed by NRG1 treatment. PTP, protein tyrosine phosphatase. (**d**) RT-qPCR detection of *CTGF* expression in ROR1 KO cells transfected with the indicated expression vectors followed by NRG1 stimulation. (**e**,**f**) IB detection of the indicated proteins (**e**) and RT-qPCR detection of *CTGF* expression (**f**) in MDA-MB-231 cells transfected with LNAs against *MAYA* followed by overexpression of the indicated plasmids and NRG1 treatment (100 ng ml^{-1} for 1 h). (**g**) Quantification of osteoclast differentiation in the presence of M-CSF only, M-CSF+RANKL, or combined M-CSF+RANKL and CM from scramble (Scr) or *MAYA* LNA-transfected BoM-1833 cells rescued with the indicated plasmids. (**h**) Measurement of helical peptides released from human bone plates incubated with primary osteoclasts treated as in **g**. For **d**,**f**,**g** and **h**, mean ± s.e.m. were derived from $n=3$ independent experiments (NS (not significant), $P>0.05$; $^{*}P<0.05$; $^{**}P<0.01$; two-tailed paired Student's *t*-test). Unprocessed original scans of all blots with size markers are shown in Supplementary Fig. 9.

well as the expression of CTGF (Fig. 8a,b). Consistently, exogenous expression of FL *MAYA*, but not the ΔLLGL2 or ΔNSUN6 mutants, in *MAYA* knockdown BoM-1833 cells rescued these phenotypes (Fig. 8b). Inducible knockdown of *MAYA* by shRNAs inhibited proliferation, migration and invasion of BoM-1833 cells (Supplementary Fig. 8b–e).

We then investigated the role of *MAYA* in breast cancer bone metastasis using the intracardiac injection experimental metastasis mouse model. Compared with control shRNA (Ctl), inducible knockdown of *MAYA* significantly decreased hindlimb tumour burden (Fig. 8c,d). Micro-computed tomography (Micro-CT) imaging revealed that mice inoculated with *MAYA* knockdown cells exhibited decreased bone lesions (Fig. 8e). Quantitative real-time RT-PCR analysis of bone tumour samples from mice inoculated with *MAYA* knockdown cells revealed a substantial decrease of *MAYA* expression (Supplementary Fig. 8f). Specimen CT revealed that *MAYA* knockdown increased trabecular bone mass in the femur (Fig. 8f). Quantification analyses confirmed a noteworthy enhancement of bone volume, trabecular thickness, and decreased trabecular spacing, but insubstantial differences in cortical bone thickness when *MAYA* was depleted (Fig. 8g–j). Histological TRAP staining indicated that *MAYA* knockdown impaired the number of osteoclasts relative to bone surface area (Fig. 8k). Therefore, these data suggest the importance of *MAYA* in promoting breast cancer metastasis to the bone.

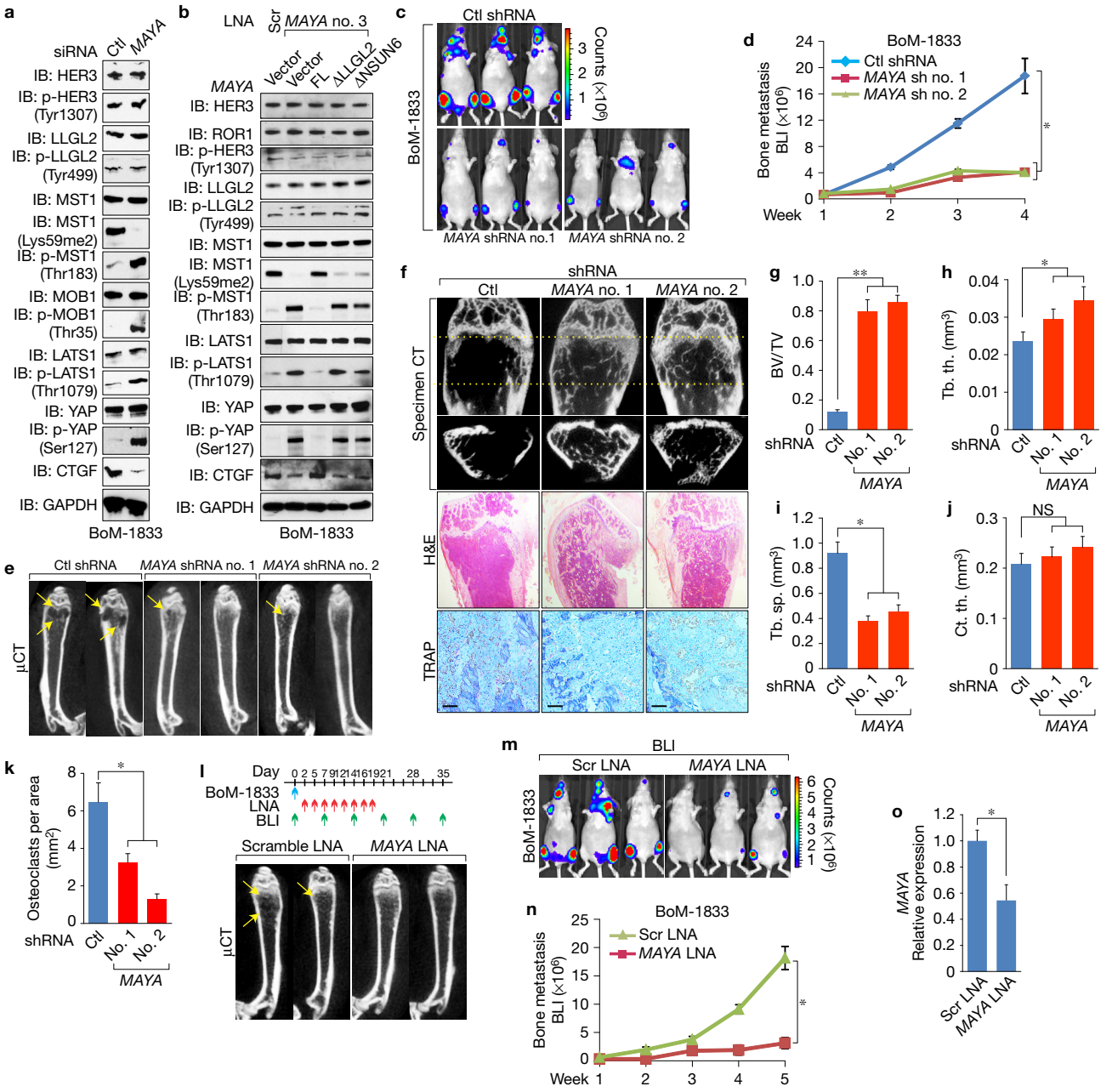

Figure 8 *MAYA* serves as a promising therapeutic target for bone metastasis. (**a**) IB detection of the indicated proteins in BoM-1833 cells transfected with *MAYA* or control siRNAs. (**b**) IB detection of the indicated proteins in BoM-1833 cells transfected with LNAs against *MAYA* followed by overexpression of the indicated plasmids and NRG1 treatment. (**c**–**f**) Representative BLI images (**c**), bone colonization (**d**), femur μCT (**e**), and specimen CT and histological images (**f**, scale bars, 200 μm) of nude mice with intracardiac injection of BoM-1833 cells harbouring the indicated shRNAs. Yellow arrows indicate tumour lesions in femur (**e**, $n = 5$ mice per group). (**g**–**j**) Quantification of bone parameters from representative specimen CT scans in **f**. BV/TV, bone volume/tissue volume ratio; Tb. th., trabecular thickness; Tb. sp., trabecular separation; Ct. th., cortical bone thickness. (**k**) Quantification of TRAP⁺ osteoclasts of histological sections from mouse femur in **f**. (**l**–**o**) Schematic diagram of LNA treatment time course (**l**, top) and femur μCT (**l**, bottom), representative BLI images (**m**), bone colonization (**n**), and RT-qPCR detection of *MAYA* expression from bone metastatic lesions (**o**) of mice with intracardiac injection of BoM-1833 cells followed by intravenous LNA administration ($n = 5$ mice per group). Yellow arrows indicate tumour lesions in the femur (**l**). For **d**,**g**–**k**,**n** and **o**, mean ± s.e.m. were derived from $n = 3$ independent experiments (NS (not significant), $P > 0.05$; $^{*}P < 0.05$; $^{**}P < 0.01$; two-tailed paired Student's *t*-test). Unprocessed original scans of all blots with size markers are shown in Supplementary Fig. 9. Statistics source data for **c**,**d**,**f**–**k** and **m**,**n** can be found in Supplementary Table 8.

Next, we examined the potential therapeutic value of *MAYA* LNAs using the same mouse model. After intracardiac inoculation of BoM-1833 cells, nude mice were intravenously injected with scramble (Scr) LNA or LNA targeting *MAYA* (15 mg kg^{-1}, three times per week) for three weeks. BLI imaging showed that the bone tumour burden was greatly reduced in mice treated with *MAYA* LNA (Fig. 8l–n). The expression level of *MAYA* from mouse bone metastatic lesions was significantly reduced following *MAYA* LNA treatment (Fig. 8o). We

further explored the tumour-promoting and bone metastasis function of *MAYA* in lung cancer using A549-Luc cells and observed similar effects (Supplementary Fig. 8g–l).

DISCUSSION

Recent studies have revealed that the activity of YAP/TAZ transcriptional co-activators and LATS1 kinase could be regulated by nutritional stress[59], GPCR signalling[51], WNT signalling[35], and the mevalonate pathway[60]. However, the modulation of the Hippo kinase MST1/2 is not yet understood. Our study found that NRG1-bound ROR1/HER3 heterodimer recruits adaptor LLGL2 and methyltransferase NSUN6 in an lncRNA-dependent fashion. The LLGL2–*MAYA*–NSUN6 module methylates MST1 at Lys59, which abolishes the kinase activity of MST1 and consequently leads to hypophosphorylation of LATS1 and YAP. YAP is activated and accumulates in the nucleus to stimulate the target gene expression involved in tumour cell proliferation and bone metastasis (Supplementary Fig. 8m).

Orphan receptor tyrosine kinase ROR1 transduces cellular signalling through both kinase-dependent and -independent mechanisms. ROR1 associates with EGFR, HER3, SRC or c-MET in response to EGF or Wnt stimulation to promote cancer cell proliferation, survival and invasion[27,46]. Our data indicate that in TNBC cells, ROR1 forms a heterodimer with HER3 to phosphorylate HER3 and LLGL2 following NRG1 stimulation. It is possible that ROR1 dynamically forms heterodimers, or heterotrimers, with other (receptor) tyrosine kinases in the presence of different ligands. ROR1 is subjected to tyrosine phosphorylation by SRC and MET within the kinase domain and proline-rich domain, respectively[46]. Although our data indicate that NRG1 exhibited minimal effect on the tyrosine phosphorylation of ROR1, it is possible that other ligands or signals may induce these modifications and regulate the kinase activity of ROR1. The downstream signalling pathways triggered by ROR1 might vary depending on the cell/tissue types. Previous studies suggested that ROR1 phosphorylates SRC to activate the AKT pathway[20,27]. Our findings demonstrated the crosstalk between ROR1–HER3 and the Hippo–YAP pathway mediated by lncRNAs under a cancer-specific context. Nuclear ErbB family members have been shown to modulate gene expression as transcriptional co-activators[61]. For example, nuclear ErbB4 has been suggested to associate with YAP and to regulate expression of YAP target genes[62]. It is possible that truncated nuclear HER3 was translocated into the nucleus to trigger the YAP transcriptional program.

The role of *MAYA* in mediating the LLGL2–NSUN6 interaction is an intriguing paradigm. The complicated secondary structure of long noncoding RNA molecules provides multiple protein binding sites, which may scaffold the RNA–protein complex formation[34,63]. Given uncharacteristic RNA-binding domains recently identified, such as WD40, SH2 and SH3 domains[64], we anticipate that lncRNA-dependent regulatory mechanisms are widely applicable in signal transduction and epigenetic modifications. Although we show that growth factor enhances the association between LLGL2, *MAYA* and NSUN6 to methylate MST1, it is worth investigating whether or not the LLGL2–*MAYA*–NSUN6 complex assembly is regulated by other ligands.

For TNBC and NSCLC patients, anti-EGFR-targeted therapies have been one of the primary treatments. However, a key challenge lies in how to overcome acquired resistance to tyrosine kinase inhibitors (TKIs). Recently, EGFR mutations have been linked to bone metastasis[65]. The highly upregulated ROR1 expression and YAP pathway activation in bone metastatic cells signified the potential therapeutic values of combined targeting of ROR1 and the YAP pathway against bone metastasis. Indeed, ROR1 has been implicated in EGFR-resistance in NSCLC patients[66]. Our observation that breast cancer patients with strong p-HER3 Tyr1307 staining exhibited unfavourable progression-free survival outcomes compared with patients with low HER3 staining suggests that p-HER3 Tyr1307 and *MAYA* may serve as predictive biomarkers to forecast bone metastasis and refer to commence targeted anti-EGFR therapy. Further, targeting ROR1 using monoclonal antibodies or small-molecule inhibitors may prove to be a promising therapeutic option for leukaemia TNBC, and NSCLC patients. Finally, our study demonstrates the effectiveness of LNA oligonucleotide-based inhibition of breast cancer bone metastasis, which could be further developed as a valuable therapeutic strategy either alone or in combination with EGFR inhibitors, to overcome resistance to EGFR-targeted therapies. □

METHODS

Methods, including statements of data availability and any associated accession codes and references, are available in the online version of this paper.

Note: Supplementary Information is available in the online version of the paper

ACKNOWLEDGEMENTS

We are grateful to J. Massague and X. Zhang for providing the MDA-MB-231 LM2 and BoM-1833 cell lines and to D. Yu for providing the MDA-MB-231-BRN and BT474-BRN cells. We thank D. Aten for assistance with figure presentation. This work was supported by National Institutes of Health Pathway to Independence Award (R00CA166527) and Cancer Prevention Research Institute of Texas First-time Faculty Recruitment Award (R1218) grants to L.Q.Y. and National Institutes of Health Pathway to Independence Award (R00DK094981) to C.R.L.

AUTHOR CONTRIBUTIONS

C.L.L. and S.W. devised and performed most experiments. K.L., J.S. and G.E.G. helped with mouse intracardiac injections. A.L., Z.X. and Q.H. helped with biochemistry studies. D.H.H. performed mass spectrometry analysis. Clinical specimens were ascertained and processed by J.Z. and Y.Z. The histological staining and corresponding analysis were performed by K.L. P.K.P. assisted with manuscript drafting. J.Y., L.H., Z.C. and H.L. performed bioinformatics analysis. S.Z. and M.-C.H. contributed to discussion and data interpretation. L.Y. and C.R.L. initiated and supervised the project and wrote the paper with input from all authors.

COMPETING FINANCIAL INTERESTS

The authors declare no competing financial interests.

Published online at http://dx.doi.org/10.1038/ncb3464
Reprints and permissions information is available online at www.nature.com/reprints

1. Guise, T. A. *et al.* Basic mechanisms responsible for osteolytic and osteoblastic bone metastases. *Clin. Cancer Res.* **12,** 6213s–6216s (2006).
2. Waning, D. L. & Guise, T. A. Molecular mechanisms of bone metastasis and associated muscle weakness. *Clin. Cancer Res.* **20,** 3071–3077 (2014).
3. Kang, Y. *et al.* A multigenic program mediating breast cancer metastasis to bone. *Cancer Cell* **3,** 537–549 (2003).
4. Pan, D. The hippo signaling pathway in development and cancer. *Dev. Cell* **19,** 491–505 (2010).
5. Harvey, K. F., Zhang, X. & Thomas, D. M. The Hippo pathway and human cancer. *Nat. Rev. Cancer* **13,** 246–257 (2013).
6. Meng, Z., Moroishi, T. & Guan, K. L. Mechanisms of Hippo pathway regulation. *Genes Dev.* **30,** 1–17 (2016).
7. Yu, F. X. & Guan, K. L. The Hippo pathway: regulators and regulations. *Genes Dev.* **27,** 355–371 (2013).
8. Hansen, C. G., Moroishi, T. & Guan, K. L. YAP and TAZ: a nexus for Hippo signaling and beyond. *Trends Cell Biol.* **25,** 499–513 (2015).

9. Zhao, B., Tumaneng, K. & Guan, K. L. The Hippo pathway in organ size control, tissue regeneration and stem cell self-renewal. *Nat. Cell Biol.* **13,** 877–883 (2011).
10. Thompson, B. J. & Sahai, E. MST kinases in development and disease. *J. Cell Biol.* **210,** 871–882 (2015).
11. Halder, G., Dupont, S. & Piccolo, S. Transduction of mechanical and cytoskeletal cues by YAP and TAZ. *Nat. Rev. Mol. Cell Biol.* **13,** 591–600 (2012).
12. Piccolo, S., Dupont, S. & Cordenonsi, M. The biology of YAP/TAZ: hippo signaling and beyond. *Physiol. Rev.* **94,** 1287–1312 (2014).
13. Bergeron, J. J., Di Guglielmo, G. M., Dahan, S., Dominguez, M. & Posner, B. I. Spatial and temporal regulation of receptor tyrosine kinase activation and intracellular signal transduction. *Annu. Rev. Biochem.* **85,** 573–597 (2016).
14. Green, J. L., Kuntz, S. G. & Sternberg, P. W. Ror receptor tyrosine kinases: orphans no more. *Trends Cell Biol.* **18,** 536–544 (2008).
15. Forrester, W. C. The Ror receptor tyrosine kinase family. *Cell. Mol. Life Sci.* **59,** 83–96 (2002).
16. Yoda, A., Oishi, I. & Minami, Y. Expression and function of the Ror-family receptor tyrosine kinases during development: lessons from genetic analyses of nematodes, mice, and humans. *J. Recept. Signal Transduct. Res.* **23,** 1–15 (2003).
17. Baskar, S. *et al.* Unique cell surface expression of receptor tyrosine kinase ROR1 in human B-cell chronic lymphocytic leukemia. *Clin. Cancer Res.* **14,** 396–404 (2008).
18. Daneshmanesh, A. H. *et al.* Orphan receptor tyrosine kinases ROR1 and ROR2 in hematological malignancies. *Leuk. Lymphoma* **54,** 843–850 (2013).
19. Zhang, S. *et al.* ROR1 is expressed in human breast cancer and associated with enhanced tumor-cell growth. *PLoS ONE* **7,** e31127 (2012).
20. Zhang, S. *et al.* The onco-embryonic antigen ROR1 is expressed by a variety of human cancers. *Am. J. Pathol.* **181,** 1903–1910 (2012).
21. Borcherding, N., Kusner, D., Liu, G. H. & Zhang, W. ROR1, an embryonic protein with an emerging role in cancer biology. *Protein Cell* **5,** 496–502 (2014).
22. Chien, H. P. *et al.* Expression of ROR1 has prognostic significance in triple negative breast cancer. *Virchows Arch.* **468,** 589–595 (2016).
23. Gentile, A., Lazzari, L., Benvenuti, S., Trusolino, L. & Comoglio, P. M. Ror1 is a pseudokinase that is crucial for Met-driven tumorigenesis. *Cancer Res.* **71,** 3132–3141 (2011).
24. Bicocca, V. T. *et al.* Crosstalk between ROR1 and the Pre-B cell receptor promotes survival of t(1;19) acute lymphoblastic leukemia. *Cancer Cell* **22,** 656–667 (2012).
25. Masiakowski, P. & Carroll, R. D. A novel family of cell surface receptors with tyrosine kinase-like domain. *J. Biol. Chem.* **267,** 26181–26190 (1992).
26. Oishi, I. *et al.* Spatio-temporally regulated expression of receptor tyrosine kinases, mRor1, mRor2, during mouse development: implications in development and function of the nervous system. *Genes Cells* **4,** 41–56 (1999).
27. Yamaguchi, T. *et al.* NKX2-1/TITF1/TTF-1-induced ROR1 is required to sustain EGFR survival signaling in lung adenocarcinoma. *Cancer Cell* **21,** 348–361 (2012).
28. Rashid, F., Shah, A. & Shan, G. Long non-coding RNAs in the cytoplasm. *Genomics Proteomics Bioinform.* **14,** 73–80 (2016).
29. Willingham, A. T. *et al.* A strategy for probing the function of noncoding RNAs finds a repressor of NFAT. *Science* **309,** 1570–1573 (2005).
30. Yoon, J. H., Abdelmohsen, K. & Gorospe, M. Posttranscriptional gene regulation by long noncoding RNA. *J. Mol. Biol.* **425,** 3723–3730 (2013).
31. Tichon, A. *et al.* A conserved abundant cytoplasmic long noncoding RNA modulates repression by Pumilio proteins in human cells. *Nat. Commun.* **7,** 12209 (2016).
32. Wang, P. *et al.* The STAT3-binding long noncoding RNA lnc-DC controls human dendritic cell differentiation. *Science* **344,** 310–313 (2014).
33. Liu, B. *et al.* A cytoplasmic NF-κB interacting long noncoding RNA blocks IκB phosphorylation and suppresses breast cancer metastasis. *Cancer Cell* **27,** 370–381 (2015).
34. Lin, A. *et al.* The LINK-A lncRNA activates normoxic HIF1α signalling in triple-negative breast cancer. *Nat. Cell Biol.* **18,** 213–224 (2016).
35. Park, H. W. *et al.* Alternative wnt signaling activates YAP/TAZ. *Cell* **162,** 780–794 (2015).
36. Mohseni, M. *et al.* A genetic screen identifies an LKB1-MARK signalling axis controlling the Hippo–YAP pathway. *Nat. Cell Biol.* **16,** 108–117 (2014).
37. Cordenonsi, M. *et al.* The Hippo transducer TAZ confers cancer stem cell-related traits on breast cancer cells. *Cell* **147,** 759–772 (2011).
38. Zanconato, F. *et al.* Genome-wide association between YAP/TAZ/TEAD and AP-1 at enhancers drives oncogenic growth. *Nat. Cell Biol.* **17,** 1218–1227 (2015).
39. Zhang, J. *et al.* YAP-dependent induction of amphiregulin identifies a non-cell-autonomous component of the Hippo pathway. *Nat. Cell Biol.* **11,** 1444–1450 (2009).
40. Gomez, M., Gomez, V. & Hergovich, A. The Hippo pathway in disease and therapy: cancer and beyond. *Clin. Trans. Med.* **3,** 22 (2014).
41. Moroishi, T., Hansen, C. G. & Guan, K. L. The emerging roles of YAP and TAZ in cancer. *Nat. Rev. Cancer* **15,** 73–79 (2015).
42. Shimo, T. *et al.* Pathogenic role of connective tissue growth factor (CTGF/CCN2) in osteolytic metastasis of breast cancer. *J. Bone Miner. Res.* **21,** 1045–1059 (2006).
43. Engelman, J. A. *et al.* MET amplification leads to gefitinib resistance in lung cancer by activating ERBB3 signaling. *Science* **316,** 1039–1043 (2007).
44. Sergina, N. V. *et al.* Escape from HER-family tyrosine kinase inhibitor therapy by the kinase-inactive HER3. *Nature* **445,** 437–441 (2007).
45. Hellyer, N. J., Kim, M. S. & Koland, J. G. Heregulin-dependent activation of phosphoinositide 3-kinase and Akt via the ErbB2/ErbB3 co-receptor. *J. Biol. Chem.* **276,** 42153–42161 (2001).
46. Gentile, A., Lazzari, L., Benvenuti, S., Trusolino, L. & Comoglio, P. M. The ROR1 pseudokinase diversifies signaling outputs in MET-addicted cancer cells. *Int. J. Cancer* **135,** 2305–2316 (2014).
47. Tao, J. J. *et al.* Antagonism of EGFR and HER3 enhances the response to inhibitors of the PI3K-Akt pathway in triple-negative breast cancer. *Sci. Signal.* **7,** ra29 (2014).
48. Bae, S. Y. *et al.* HER3 status by immunohistochemistry is correlated with poor prognosis in hormone receptor-negative breast cancer patients. *Breast Cancer Res. Treat.* **139,** 741–750 (2013).
49. Yaffe, M. B. Phosphotyrosine-binding domains in signal transduction. *Nat. Rev. Mol. Cell Biol.* **3,** 177–186 (2002).
50. Johnson, R. & Halder, G. The two faces of Hippo: targeting the Hippo pathway for regenerative medicine and cancer treatment. *Nat. Rev. Drug Discov.* **13,** 63–79 (2014).
51. Yu, F. X. *et al.* Regulation of the Hippo-YAP pathway by G-protein-coupled receptor signaling. *Cell* **150,** 780–791 (2012).
52. Haag, S. *et al.* NSUN6 is a human RNA methyltransferase that catalyzes formation of m5C72 in specific tRNAs. *RNA* **21,** 1532–1543 (2015).
53. Xing, Z. *et al.* lncRNA directs cooperative epigenetic regulation downstream of chemokine signals. *Cell* **159,** 1110–1125 (2014).
54. Glantschnig, H., Rodan, G. A. & Reszka, A. A. Mapping of MST1 kinase sites of phosphorylation. Activation and autophosphorylation. *J. Biol. Chem.* **277,** 42987–42996 (2002).
55. Sapru, M. K. Neuregulin-1 regulates expression of the Ets-2 transcription factor. *Life Sci.* **69,** 2663–2674 (2001).
56. Minn, A. J. *et al.* Genes that mediate breast cancer metastasis to lung. *Nature* **436,** 518–524 (2005).
57. Zhang, C. & Yu, D. Microenvironment determinants of brain metastasis. *Cell Biosci.* **1,** 8 (2011).
58. Zhang, S. *et al.* SRC family kinases as novel therapeutic targets to treat breast cancer brain metastases. *Cancer Res.* **73,** 5764–5774 (2013).
59. Wang, W. *et al.* AMPK modulates Hippo pathway activity to regulate energy homeostasis. *Nat. Cell Biol.* **17,** 490–499 (2015).
60. Sorrentino, G. *et al.* Metabolic control of YAP and TAZ by the mevalonate pathway. *Nat. Cell Biol.* **16,** 357–366 (2014).
61. Lin, S. Y. *et al.* Nuclear localization of EGF receptor and its potential new role as a transcription factor. *Nat. Cell Biol.* **3,** 802–808 (2001).
62. Haskins, J. W., Nguyen, D. X. & Stern, D. F. Neuregulin 1-activated ERBB4 interacts with YAP to induce Hippo pathway target genes and promote cell migration. *Sci. Signal.* **7,** ra116 (2014).
63. Xue, Z. *et al.* A G-rich motif in the lncRNA braveheart interacts with a zinc-finger transcription factor to specify the cardiovascular lineage. *Mol. Cell* **64,** 37–50 (2016).
64. Castello, A. *et al.* Insights into RNA biology from an atlas of mammalian mRNA-binding proteins. *Cell* **149,** 1393–1406 (2012).
65. Bittner, N. *et al.* Bone metastases and the EGFR and KRAS mutation status in lung adenocarcinoma–the results of three year retrospective analysis. *Pathol. Oncol. Res.* **21,** 1217–1221 (2015).
66. Karachaliou, N. *et al.* ROR1 as a novel therapeutic target for EGFR-mutant non-small-cell lung cancer patients with the EGFR T790M mutation. *Transl. Lung Cancer Res.* **3,** 122–130 (2014).

METHODS

Clinical samples. Fresh frozen breast carcinomas and their adjacent normal tissues were purchased from Asterand Bioscience. Breast cancer, lung cancer and multiple cancer type tissue microarrays were purchased from US Biomax, Biochain, and US BioLab. The fresh frozen primary tumour and normal breast tissues (Yixin Bre-01 cohort) were obtained from Yixing People's Hospital in China. The study protocol was approved by the Institutional Review Board of Nanjing Medical University (Nanjing, China). All tissue samples were collected in compliance with informed consent policy. Clinical tissue information for all data presented in Figs 1c,d, 2k–m and 4c–e and Supplementary Figs 2l,m and 4e–g is summarized in Supplementary Table 1.

Cell culture, treatment, transfection, electroporation and lentiviral transduction. Human breast cancer cells MDA-MB-231 (ATCC), MCF-7 (ATCC), MDA-MB-231-BRN, BT474 and BT474-BRN (provided by D. Yu at MD Anderson Cancer Center) were maintained in Dulbecco's modified Eagle's medium (DMEM)/F12 with 5% fetal bovine serum (FBS), and 1% penicillin/streptomycin (pen/strep). The TEAD-reporter-containing MCF-7 cell line (BPS Bioscience) was cultured according to the vendor's instructions. MDA-MB-231-LM2 and MDA231-BoM-1833 were provided by X. Zhang (Baylor College of Medicine) and maintained in DMEM (Life Technologies) with 10% FBS and 1% pen/strep. Human non-small cell lung cancer cells A549 and A549-Luc luciferase-expressing cells (Caliper Life Sciences) were maintained in RPMI 1640 with 10% FBS and 1% pen/strep. Mouse lymphoblast cell line 32D Clone 3 (ATCC CRL11346) was maintained in RPMI 1640 with 4.5 g l^{-1} glucose, 10% FBS and 10% mouse interleukin-3 culture supplement. All cell lines were authenticated by autosomal STR profiles provided by the MDACC Characterized Cell Line core. MDA-MB-231, MCF-7, MDA-MB-231-BRN, BT474 and BT474-BRN, MDA-MB-231-LM2 and MDA231-BoM-1833 cell lines were tested negative for mycoplasma by the MDACC Characterized Cell Line core. The TEAD-reporter-containing MCF-7 cell line has been screened using the PCR-based VenorGeM Mycoplasma Detection kit to confirm the absence of mycoplasma by BPS Bioscience. A549 and A549-Luc luciferase-expressing cells are confirmed to be pathogen free by the IMPACT Profile I (PCR) at the University of Missouri Research Animal Diagnostic and Investigative Laboratory as indicated by the vendor. The 32D cell line was assayed for mycoplasma, by Hoechst stain, PCR and the standard culture test by ATCC. None of the cell lines used was found in the database of commonly misidentified cell lines that is maintained by ICLAC and NCBI Biosample.

For treatment, cells were serum starved overnight to 24 h followed by treatment with growth factors (PeproTech), EGF (10 ng ml^{-1}), NRG1 (100 ng ml^{-1}) or LPA (1 μM, Cayman Chemical) for 30 min or 2 h. Under the specified conditions, cells were pre-treated with the pan-EGFR inhibitor dacomitinib (PF299804, PF299) at 100 nM, the c-SRC inhibitor saracatinib (AZD0530) and the c-MET inhibitor JNJ-38877605 (Selleckchem) at 5 μM for 2 h.

siRNA or LNA transfections were performed using DharmaFECT4 (GE Healthcare). Plasmid transfections were performed using Lipofectamine 3000 (Life Technologies). Electroporation of 32D cells with DNA plasmids was performed using the Amaxa 4D-Nucleofector System. Lentiviruses were produced in HEK293T cells with the ViraPower Lentiviral Expression System (Life Technologies) and used to transduce target cells.

Plasmids and constructs. The FL LLGL2, MST1, NSUN6, BCAR3, HER3 and ROR1 mammalian expression vectors were obtained from Origene Technologies. Bacterial expression vectors for His_6-HER3 (WT and mutants) and HER3 ICD were constructed by subcloning the corresponding gene sequences into pET-DEST42 vectors using the Gateway system (Life Technologies). GST-tagged LLGL2 (WT and mutants) was constructed into the pGEX-5X-1 backbone (GE Healthcare). Mammalian expression vectors for FL *MAYA* and mutants were constructed by subcloning the gene sequences into the pBabe backbone (Addgene). To generate the LNA no. 3-resistant *MAYA* mammalian expression vectors used in the rescue experiments, LNA no. 3-targeting sequences GAG CCT TTG CAA AGA G were mutated to GAG CCT TTC GTA AGA G. All mutants were generated using the QuikChange Lightning Site-Directed Mutagenesis Kit (Agilent Technologies).

Antibodies. The antibodies used in this study are summarized in Supplementary Table 6. The specificity of the antibodies was confirmed by peptide competition assay with unphosphorylated/unmethylated peptide, phosphorylated/methylated peptide, or corresponding scrambled phosphorylated/methylated peptide (modified residue was exchanged in position with its adjacent residue).

Generation of knockout cell lines. CRISPR–Cas9 KO double nickase plasmids of ROR1 (h, sc-401841-NIC), HER3 (h, sc-400146-NIC), LLGL2 (h, sc-404667-NIC) and NSUN6 (h, sc-415118-NIC) were used to generate stable knockout cell lines of MDA-MB-231 and BoM-1833 according to the manufacturer's instructions. Either individual or pooled single-cell clones with efficient target gene KO (as indicated in the figures) were used for downstream functional experiments to minimize the clonal variation.

siRNA, shRNA and LNA. Lincode siRNA library (G-301005-01), Lincode SMARTpool siRNA targeting *MAYA* (R-036866), Lincode non-targeting control siRNAs (D-001320), and ON-TARGETplus SMARTpool siRNA targeting *ROR1* (L-003171), *BCAR3* (L-011469), *LLGL2* (L-019812), *HER3* (L-003127), *EGFR* (L-003114), *NSUN6* (L-018822) and *DOT1L* (L-014900) from GE Healthcare Dharmacon were used in this study. The knockdown efficiency and specificity of all siRNAs were validated by either RT-qPCR or immunoblotting. The shRNAs targeting *MAYA* were designed using the shERWOOD algorithm and cloned into the UltramiR scaffold in the pZIP lentiviral vector (transOMIC technologies). For *in vivo* inducible knockdown of *MAYA* in xenograft experiments, shRNA sequences were constructed into the pZIP-TRE3GS lentiviral vector (transOMIC technologies). LNAs targeting *MAYA* or a scrambled sequence were designed and synthesized from Exiqon. Supplementary Table 7 contains detailed sequence information for siRNAs, shRNAs and LNAs.

Protein recombination and purification. GST-LLGL2, GST-MST1, BCAR3 and GST-RASSF1 were obtained from Abnova. FLAG-NSUN6, FLAG-SAV1, FLAG-MST1, FLAG-ROR1 (WT and extracellular domain) and FLAG-HER3 were obtained from Origene Technologies. His_6-MOB1 was purchased from Novoprotein Inc. GST-ROR1 was obtained from SignalChem. His_6-HER3 intracellular domain (ICD) and WT His_6-MST1 and corresponding mutants were expressed in the *E. coli* strain BL21-CodonPlus (DE3)-RIPL (Agilent Technologies) and purified using HisPur Cobalt Spin Columns (Life Technologies). Domain deletion or point mutants of GST-ROR1 ICD and GST-LLGL2 were purified using the Pierce GST Spin Purification Kit (Life Technologies). Biotinylated HER3 and phospho-HER3 peptides were synthesized by Elim Biopharmaceuticals Inc.

Cell lysis, fractionation, immunoprecipitation and immunoblotting. Cells lysis preparation, immunoprecipitation and immunoblotting were performed as previously described[34,53]. For cell fractionation, cytoplasmic and nuclear fractions were separated using a cytoplasmic and nuclear protein/RNA extraction kit (Thermo Fisher Scientific) following the manufacturer's instructions.

Human CTGF ELISA. The human CTGF levels in the conditioned media of cultured cells were quantitatively determined in triplicate by the OmniKine ELISA kit (Assay Biotechnology).

***In vitro* osteoclast differentiation.** Human osteoclasts were obtained from Lonza and differentiated *in vitro* according to the vendor's instructions. Conditioned media collected from the KO cells or cells transfected with indicated LNAs/plasmids after 72 h were added to osteoclast cells at day 3 of differentiation in a 6-well plate. In rescue experiments, recombinant CTGF or CCN3 (PeproTech) was supplemented in conditioned media as indicated. Cells were TRAP stained on day 7 using the Acid Phosphatase, Leukocyte (TRAP) kit (Sigma-Aldrich), and TRAP+-multinucleated cells were quantified as mature osteoclasts. Quantitative TRAP assay was performed using the TRACP and ALP assay kit (Takara). For osteoclast resorption function analyses, bone marrow osteoclast differentiation was conducted in OsteoAssay bone plates (Lonza) and osteoclast activity was determined by quantifying the type I collagen helical peptide α1 (I) 620–633 released from bone into culture medium using the MicroVue Bone Helical Peptide EIA assay (Quidel).

Tumour bone metastasis analysis. All animal experiments were performed in accordance with protocols approved by the Institutional Animal Care and Use Committee of MD Anderson. Animals arriving in our facility were randomly put into cages with five mice each. They were implanted with respective tumour cells in the unit of cages, which were randomly selected. The animal experiment was set up to use 5–10 mice per group to detect a twofold difference with a power of 80% and at the significance level of 0.05 by a two-sided test for significant studies (RaoSoft Inc. sample size calculator). The luciferase-labelled BoM-1833 or A549-Luc cells (2×10^5) in 50 μl 1× PBS were intracardially injected into the left ventricle of nu/nu, female 4–6-week-old nude mice using a 100-μl Hamilton Microliter syringe. To induce *MAYA* shRNA expression, mice were fed with 1 mg ml^{-1} of tetracycline in drinking water containing 2% sucrose.

To assess the effect of *MAYA* knockdown with LNA, mice were intravenously injected with *in vivo*-grade LNAs against *MAYA* (Exiqon) in PBS (15 mg kg^{-1}) three times per week for three weeks after BoM-1833 cells injection. Bone metastases were quantified by BLI every week using an IVIS Spectrum Xenogen Imaging System (Caliper Life Sciences). The osteolytic metastatic lesions on the femurs and tibiae were visualized using the micro-CT imaging. The hindlimbs or other organs were removed and fixed for histological analysis. For the structural analysis of trabecular

DOI: 10.1038/ncb3464

and cortical bones, mouse femurs and tibias were fixed in 70% ethanol and scanned at 7 μm resolution using the eXplore Locus micro-computed tomography instrument (μCT, GE Healthcare) at the Small Animal Imaging Facility of MDACC. The images were reconstructed and trabecular bone parameters were calculated using the eXplore Utilities software (GE Healthcare). For all animals producing respective tumours, they were randomly divided into groups. No animals were excluded from the analysis. The investigators were not blinded to allocation during experiments and outcome assessment.

RNAi screening. Dharmacon Lincode SMARTpool siRNA Library-Human NR LncRNA RefSeq v54 (no. G-301000) (GE Dharmacon) was used. TEAD-reporter-MCF-7 cells (1×10^4) were plated in 96-well plates 24 h before transfection. The cells were transfected with either the 15 pmol Lincode siRNA library or siRNA control (GE Healthcare Dharmacon). siGLO green transfection indicator was included to show that over 80% of the cells were transfected using this method. Cells were lysed 72 h after transfection and assayed for luciferase activity using the Dual-Glo Luciferase reporter system (Promega) and activities were monitored by Synergy H4 Hybrid Multi-Mode Microplate Reader (BioTek). The protein concentrations of diluted cell lysates (1:100) were measured in parallel using the Bio-Rad protein assay kit (Bio-rad), which was used to normalize the luciferase activity. The firefly luciferase activity for each 96-well plate was subtracted with background, normalized by protein concentration, and further normalized by control siRNA as fold changes. Log_2 of relative fold changes were plotted. The hits with $\log_2 \leq -3$ were selected as the top candidates.

RNA biology assays. The *in vitro* transcription, RNA pulldown/mass spectrometry analysis, *in vitro* RNA–protein binding assay, *in vitro* RNA pulldown coupled with dot-blot assay and RT-qPCR were performed as previously described[34,53]. The RNA electrophoretic mobility shift assay was performed as previously described[34,53] using bacterial recombinant LLGL2 and NSUN6 with synthesized RNA oligonucleotides corresponding to nucleotides 241–300 and nucleotides 841–900 (GE Healthcare Dharmacon). 5′- and 3′-rapid amplification of cDNA ends (RACE) was performed using the SMARTer RACE 5′/3′ Kit (Clontech). *MAYA* RNA expression was detected using the NorthernMax Kit (Ambion) with biotin-labelled LNA probes (Exiqon) in cells and using a pre-made human tissue northern blot (Zyagen). Supplementary Table 7 contains detailed sequence information for primers and probes.

RNAScope assay, immuno-RNA FISH and histological analysis/microscopy. Detection of *MAYA* expression using the RNAScope probe (designed by Advanced Cell Diagnostics) was performed on breast or lung cancer cell lines and tissue microarrays with the RNAScope 2.0 High Definition Assay kit according to the manufacturer's instructions (Advanced Cell Diagnostics). The images were visualized with the Zeiss Axioskop2 plus Microscope, and the slides were scanned on the Automated Cellular Image System III (ACIS III, Dako) for quantification by digital image analysis.

Immuno-RNA FISH was performed as previously described[34]. In brief, the specimen slides from RNA FISH were blocked with blocking buffer (1× PBS/5% goat serum/0.3% Triton X-100) for 1 h at room temperature followed by incubation with diluted primary antibody in dilution buffer (1× PBS/1% BSA/0.3% Triton X-100) for 2 h at room temperature, then incubated with fluorochrome-conjugated secondary antibody for 1 h at room temperature in the dark, and the slides were rinsed and mounted for visualization.

Immunohistochemistry (IHC) staining was performed as previously described[34,53]. For Von Kossa staining, slides were stained in 1% silver nitrate followed by a wash, then incubated in formaldehyde, sodium carbonate solution to develop the stain followed by a wash, then placed in 5% sodium thiosulfate solution and rinsed. The slides were counterstained in van Gieson stain. For tartrate-resistant acid phosphatase (TRAP) staining, slides were incubated in acetate buffer of sodium acetate and tartaric aid, pH 5.0 at 37 °C for 20 min; then the substrate naphthol AS-MX phosphate was added, followed by the colour developer, fast red TR hemi (zinc chloride) salt at 37 °C until colour development was observed in TRAP-positive cells. The slides were washed and counterstained in Harris's haematoxylin. Images were acquired with the Zeiss Axioskop2 plus microscope and analysed with ProgRes Capture Pro software. The slides were scanned on the Automated Cellular Image System III (Dako, Agilent) for quantification by digital image analysis.

Image analysis and quantification for RNAScope assay and immunohistochemistry. A total score of *MAYA* expression was calculated from both the percentage of positive cells and intensity. High and low expression was defined using the mean score of all samples as a cutoff point. Spearman rank correlation was used for statistical analyses of the correlation between each marker and clinical stage. The RNAScope and IHC staining were categorized into five grades 0, 1+, 2+, 3+ and 4+, according to the following criteria: 0) no staining or less than 5% tumour cells in each field (three fields) examined; 1+) 5%–10% tumour cells have staining in each field (three fields) examined; 2+) 10%–25% tumour cells have staining in each field (three fields) examined; 3+) 25%–50% tumour cells have staining in each field (three fields) examined; 4+) 50%–100% tumour cells have staining in each field (three fields) examined. If the staining score was $\geq 2+$, we considered this case to be *MAYA* positive. The positive staining percentages for *MAYA* over total case number were averaged and shown. For quantification analysis of RNAScope signal and IHC staining, the staining density for each tissue sample was determined by Image-Pro plus 6.0 (Media Cybernetics) and calculated on the basis of the average staining intensity and the percentage of positively stained cells.

***In vitro* kinase assay.** WT or mutant substrate proteins were incubated with 50 μl of *in vitro* kinase assay buffer I (SignalChem) containing 100 μM ATP (cold reaction) or 10 μCi [γ-^{32}P]ATP and the indicated protein kinase for 1 h at 30 °C. To recover the phosphorylated GST-tagged protein, Pierce Glutathione Magnetic Beads (Millipore) were added into reactions and the bound proteins were washed and eluted according to the vendor's instructions. The eluted proteins were dialysed against the appropriate buffers for downstream assays or separated by SDS–PAGE and detected by Coomassie blue staining, autoradiography or immunoblotting.

***In vitro* methylation assay.** Purified recombinant proteins were incubated (1 h, 30 °C) with 1 μg of recombinant FLAG-NSUN6 in 30 μl of methylation buffer (50 mM HEPES pH 8.0, 0.01% (v/v) NP-40, 10 mM NaCl, 1 mM dithiothreitol, and 1 mM phenylmethylsulfonyl fluoride) supplemented with 2 μl of *S*-adenosyl-L-[methyl-[^{3}H]methionine ([^{3}H]-SAM, Perkin Elmer; for radioactive methylation) or 20 nmol of *S*-adenosyl-L-methionine sulfate *p*-toluenesulfonate (SAMe-PTS, Sigma-Aldrich; for non-radioactive methylation). SDS loading buffer was added to methylation reactions and boiled followed by separation on a 4–12% SDS–PAGE gel. The resulting protein bands were visualized by Coomassie blue staining, immunoblotting or autoradiography using EN3HANCE spray (Perkin Elmer).

ChIP and RIP assays, cell proliferation assay, migration and invasion assays. Cell fixation and chromatin preparation were performed using truChIP Chromatin Shearing Kits on the Covaris M220 focused Ultrasonicator (Covaris). The downstream procedure for ChIP was conducted as previously described[53]. RIP assay, cell proliferation, migration and invasion assays were performed as previously described[34].

Computational analysis of TCGA RNA-Seq data. We downloaded the breast cancer RNA-seq BAM files from the UCSC Cancer Genomics Hub (CGHub, https://cghub.ucsc.edu). Quantification and statistical analysis of *MAYA* expression were performed as previously described[34].

Statistics and reproducibility. The experiment was set up to use 3–5 samples/repeats per experiment/group/condition to detect a twofold difference with a power of 80% and at the significance level of 0.05 by a two-sided test for significant studies. All experiments including IP/IB and immuno-FISH were carried out with three biological replicates. Panels in Figs 1d,h–l, 2l, 4c,k,l, 5h and 8c,d,f–k,m,n and Supplementary Figs 1i–l, 2i–l, 6e–h, 7j and Supplementary Fig. 8d,e,i–l show a representative image of three independent experiments. Analyses of relative gene expression were determined using the $2\text{-}\Delta\Delta Ct$ method with *GAPDH* or *B2M* as the internal reference genes. The relative quantities of ChIP samples were normalized by individual inputs, respectively. Results are reported as mean ± standard error of the mean (s.e.m.) of at least three independent experiments. Each exact *n* value is indicated in the corresponding figure legend or in the figure. Statistical analysis was performed using GraphPad Prism 7 software. Comparisons were analysed by two-tailed paired Student's *t*-test, Wilcoxon test or one-way ANOVA test (not significant (NS), $P > 0.05$, $^*P < 0.05$, $^{**}P < 0.01$ and $^{***}P < 0.001$), as indicated in the individual figures. Fisher's exact test was implemented for statistical analyses of the correlation between markers and clinical parameters. For survival analysis, the expression of *MAYA* or phosphorylation density of indicated proteins was treated as a binary variant and divided into 'high' and 'low' level. Kaplan–Meier survival curves were compared using the log rank test. The experiments were not randomized. The investigators were not blinded to allocation during experiments and outcome assessment.

Data availability. The breast cancer RNA-seq data used to analyse *MAYA* expression were derived from the TCGA Research Network: http://cancergenome.nih.gov, and the breast cancer RNA-seq BAM files were downloaded from the UCSC Cancer Genomics Hub (CGHub, https://cghub.ucsc.edu; also available from http://xena.ucsc.edu/public-hubs/). Source data for all mass spectrometry experiments (Fig. 2a and Supplementary Figs 2a, 3a,b,e and Supplementary Fig. 4a) have been provided as Supplementary Table 2, 3 and Supplementary Table 5. Statistics source data for Figs 1d,h–l, 2l, 4c,k–l, 5h and 8c,d,f–k,m,n and Supplementary Figs 1i–l, 2i–l, 6e–h, 7j and 8d,e,i–l have been provided in Supplementary Table 8. All other data supporting the findings of this study are available from the corresponding author on request.

nature cell biology

DOI: 10.1038/ncb3464

In the format provided by the authors and unedited.

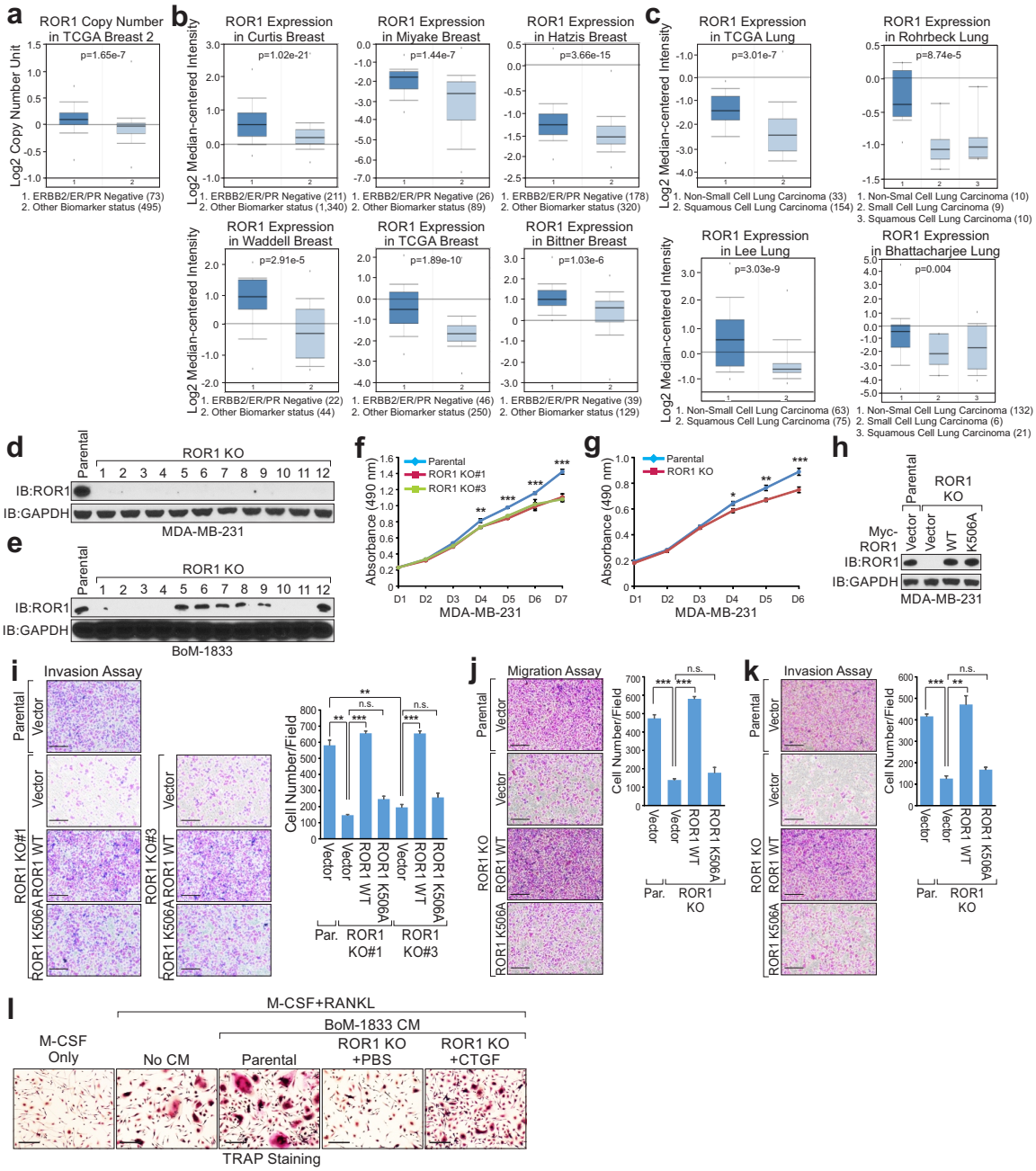

Supplementary Figure 1 ROR1 promotes proliferation and mobility of breast cancer cells. (a) Oncomine box plot showing ROR1 copy numbers in human ERPR-/HER2- triple negative breast cancer (TNBC) and non-TNBC subtypes (n=73 and 495 tumors respectively, one-way ANOVA). (b) Oncomine box plots showing ROR1 expression levels in a series of human TNBC (n=211, 178, 46, 26, 22 and 39 tumors, one-way ANOVA) and non-TNBC subtypes (n=1,340, 320, 250, 89, 44 and 129 tumors, one-way ANOVA). (c) Oncomine box plots showing ROR1 expression levels in human Non-small Cell Lung Carcinoma (n=33, 63, 10, 26, and 132 tumors, one-way ANOVA) and Small cell lung carcinoma (n=9 and 6 tumors, one-way ANOVA) or squamous cell lung carcinoma cohorts (n=154, 75, 10, 26, and 21 tumors, one-way ANOVA). (d and e) Immunoblotting (IB) of indicated proteins in parental/ROR1 KO MDA-MB-231 (d) and BoM-1833 (e) single cell clones. (f and g) Cell proliferation assay of individual (f) and pooled (g) clones of ROR1 KO MDA-MB-231 cells. (h) IB detection of indicated proteins in ROR1 KO cells expressing WT ROR1 or K506A mutant. (i) Cell invasion assay of ROR1 KO MDA-MB-231 cells with expression of indicated plasmid (left, scale bars: 200 μm; right, quantification). (j and k) Cell migration (j) and invasion (k) assay of pooled clones of ROR1 KO MDA-MB-231 cells with overexpression of indicated plasmid (scale bars: 200 μm). (l) TRAP staining showing the osteoclast differentiation in the presence of M-CSF only, M-CSF+RANKL, or combined M-CSF+RANKL and conditioned media (CM) from ROR1 KO BoM-1833 cells or CM from ROR1 KO BoM-1833 cells KO supplemented with PBS or recombinant CTGF (50 ng ml^{-1}) (scale bars: 200 μm). For a-c, the boxes show the median±1 quartile, with whiskers extending to the most extreme data point within 1.5 interquartile ranges from the box boundaries. For f, g and i-k, mean ± s.e.m. were derived from n=3 independent experiments (n.s., p>0.05, *p<0.05 and **p<0.01, ***p<0.001, two-tailed paired Student's t-test). Unprocessed original scans of all blots with size marker are shown in Supplementary Fig. 9. Statistics source data for i-l are in Supplementary Table 8.

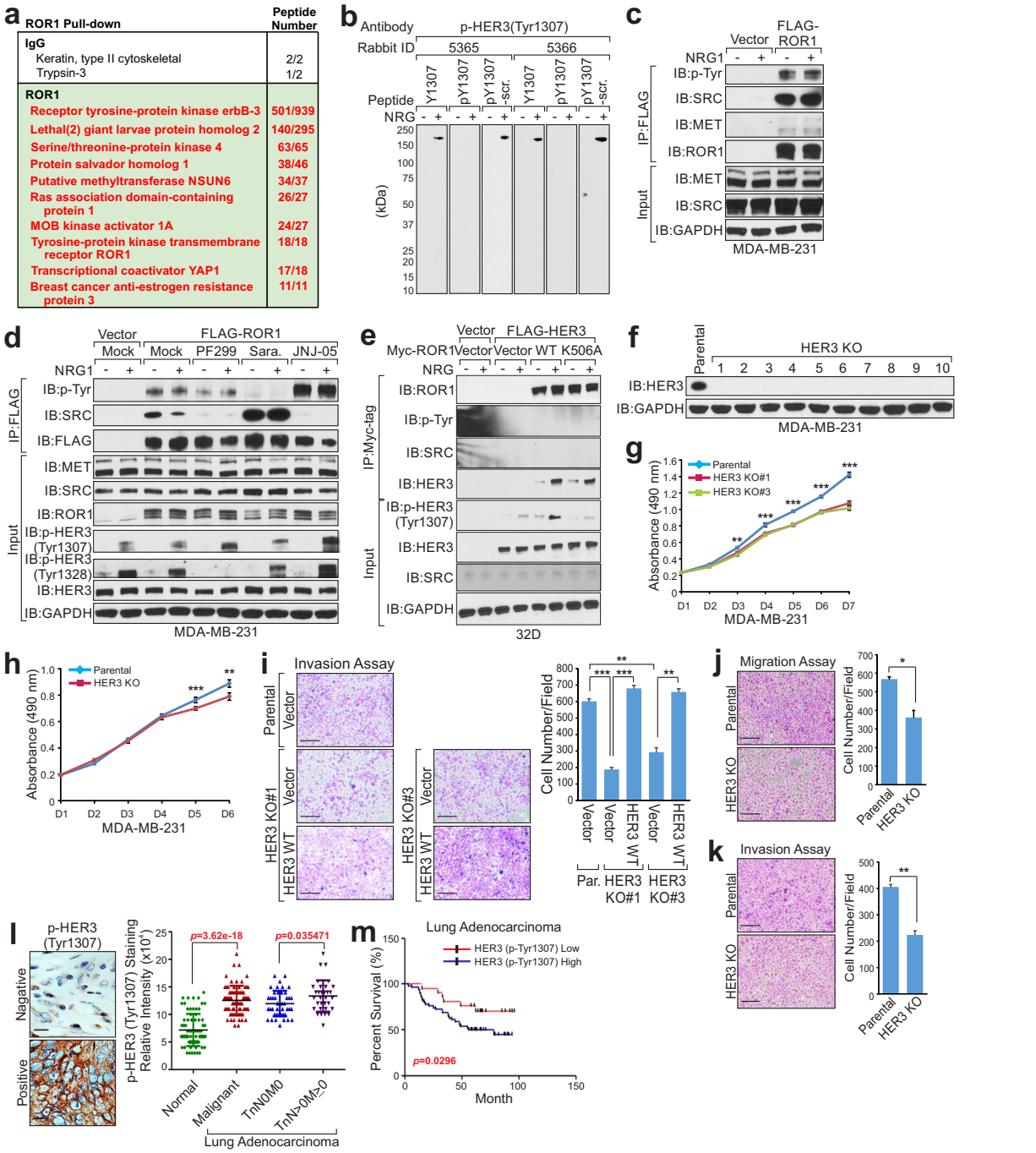

Supplementary Figure 2 Identification of ROR1-associated proteins, characterization of ROR1 phosphorylation and examination of the role of p-HER3 (Tyr1307) in breast and lung cancer. (a) A list of top ROR1-associated proteins identified by protein pull-down and MS in MDA-MB-231 cells. (b) IB detection of p-HER3 (Tyr1307) in MDA-MB-231 cells treated with or without NRG1 using antibodies pre-incubated with indicated blocking peptides. Antibodies generated from two independent rabbits were tested. (c and d) Immunoprecipitation (IP) and IB detection of indicated proteins in MDA-MB-231 cells transfected with indicated plasmids (c) or treated with indicated small compound inhibitors (d) followed by NRG1 treatment. (e) IP and IB detection of indicated proteins in 32D cells transfected with indicated expression vectors followed by NRG1 stimulation. (f) IB detection of indicated proteins in parental/HER3 KO MDA-MB-231 single cell clones. (g and h) Cell proliferation assay of individual (g) and pooled (h) clones of HER3 KO MDA-MB-231 cells. (i) Cell invasion assay of individual clones of HER3 KO MDA-MB-231 cells with overexpression of indicated plasmid (left, scale bars: 200 μm; right, quantification). (j and k) Cell migration (j) and invasion (k) assay of pooled clones of HER3 KO MDA-MB-231 cells (left, scale bars: 200 μm; right, quantification). (l) Immunohistochemical (IHC) staining of p-HER3 (Tyr1307) in normal lung tissues, lung adenocarcinomas, non-metastatic (TnN0M0) and metastatic (TnN>0M≥0) lung adenocarcinomas (left, scale bars: 40 μm; right, n=75, 75, 43 and 32 lung tissues/adenocarcinomas respectively, median, one-way ANOVA). (m) Kaplan-Meier survival analysis of p-HER3 (Tyr1307) low and high lung adenocarcinoma patients (n=20 and 55 patients respectively, log rank test). For g-k, mean ± s.e.m. were derived from n=3 independent experiments (*p<0.05, **p<0.01 and ***p<0.001, two-tailed paired Student's t-test). Unprocessed original scans of all blots with size marker are shown in Supplementary Fig. 9. Statistics source data for i-l are in Supplementary Table 8.

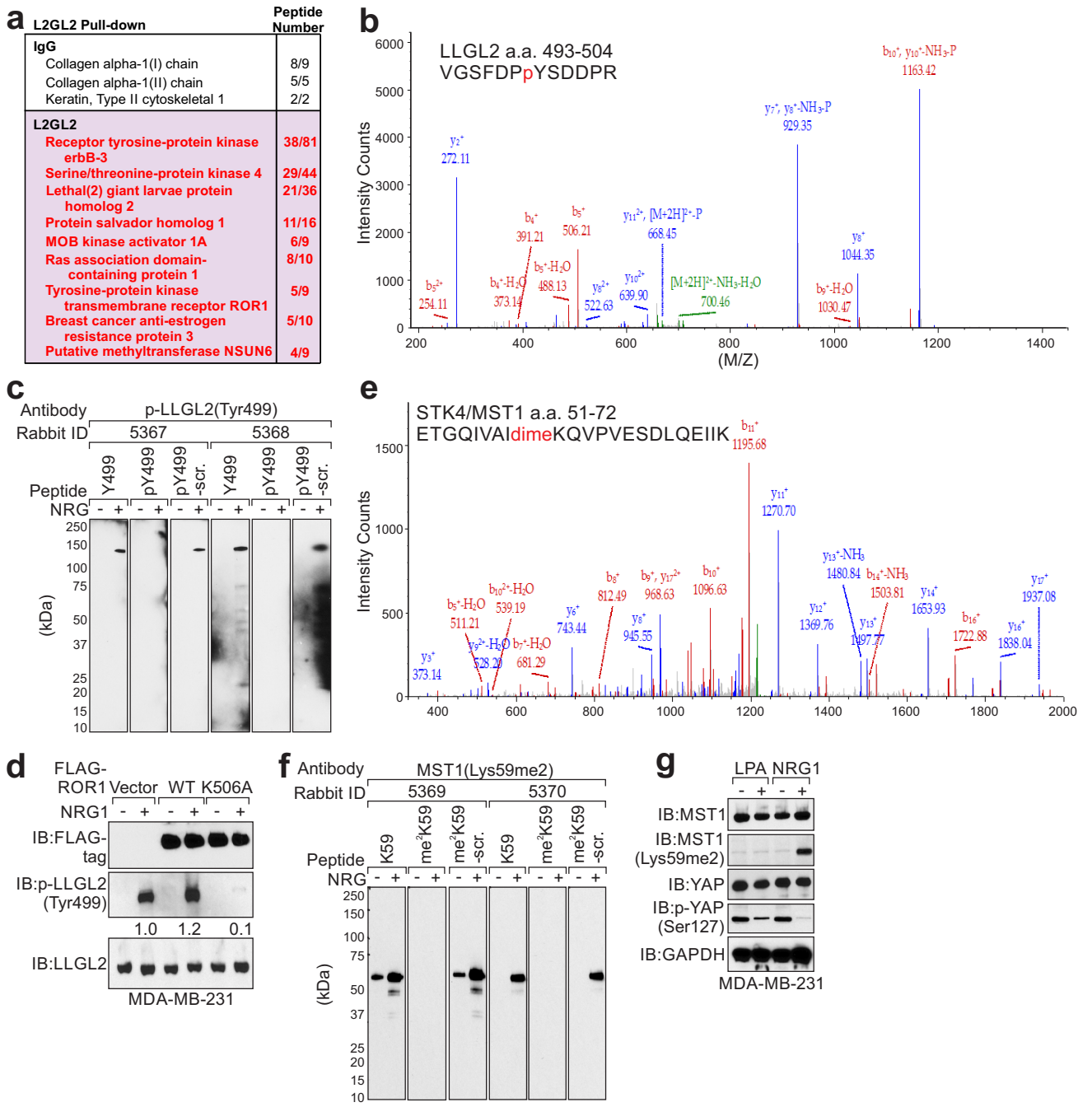

Supplementary Figure 3 Identification and characterization of p-LLGL2 (Tyr499) and MST1 (Lys59me2). (a) Summary of top LLGL2-associated proteins identified by LLGL2 pull-down followed by MS in MDA-MB-231 cells. (b and e) Annotated MS/MS spectrum assigned to the LLGL2 peptide VGSFDP[p]YSDDPR, at 717.782 Da. (b) and the STK4/MST1 peptide ETGQIVAI[dime] KQVPVESDLQEIIK, at 1233.200 Da. (e). Data acquired from analysis of the tryptic digest by high-sensitivity LC-MS/MS on an Orbitrap Elite high-resolution mass spectrometer. (c and f) IB detection of p-LLGL2 (Tyr499) (c) and MST1 (Lys59me2) (f) in MDA-MB-231 cells treated with or without NRG1, using antibodies pre-incubated with indicated blocking peptides. Antibodies generated from two independent rabbits were tested. (d) IB detection of indicated proteins in cells transfected with indicated expression vectors followed by NRG1 stimulation. Scanning densitometric analysis was performed for p-LLGL2 (Tyr499) blot. (g) IB detection of indicated proteins in MDA-MB-231 cells treated with LPA or NRG1. Unprocessed original scans of all blots with size marker are shown in Supplementary Fig. 9.

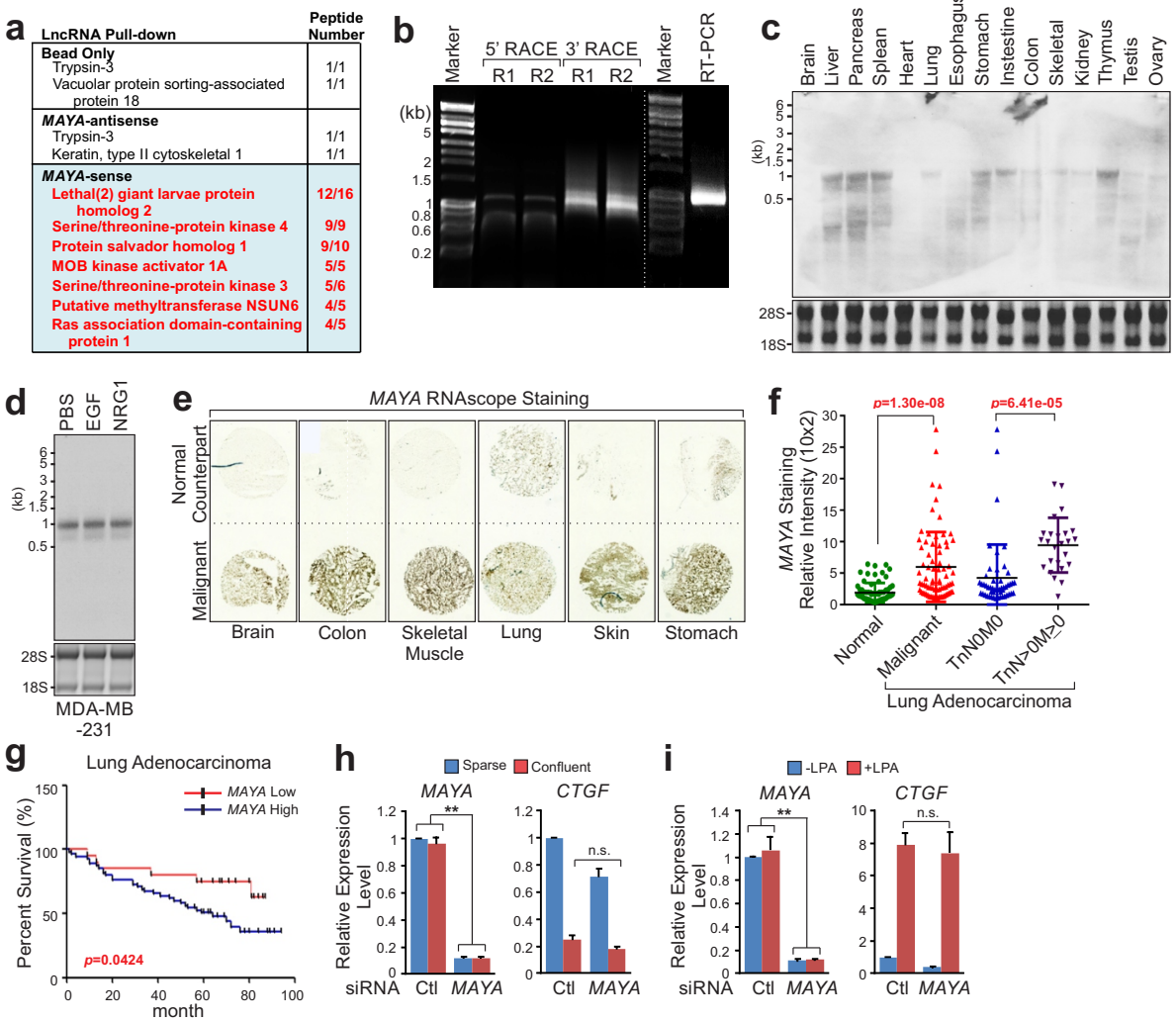

Supplementary Figure 4 Identification of *MAYA*-associated proteins, characterization of *MAYA* transcript and its correlation with lung cancer. (a) Summary of the top *MAYA*-associated proteins identified by RNA pull-down followed by MS in MDA-MB-231 cells. (b) Determination of *MAYA* transcript in MDA-MB-231 cells by 5'- and 3'-RACE. R1: repeat 1, R2: repeat 2. (c) Top, northern blot detection of *MAYA* in pre-made human tissue RNA blots; bottom, RNA gel electrophoresis. (d) Top, northern blot detection of *MAYA* in MDA-MB-231 cells with indicated treatment; bottom, RNA gel electrophoresis. (e) Examination of MAYA expression in multiple tumor types and their normal counterparts by RNAscope® assay. (f) *MAYA* RNAscope® staining intensities in normal lung tissues, lung adenocarcinomas, non-metastatic (TnN0M0) and metastatic (TnN>0M≥0) lung adenocarcinomas (n=75, 75, 50 and 25 lung tissues/ adenocarcinomas respectively, median, one-way ANOVA). (g) Kaplan-Meier survival analysis of *MAYA* low and high lung cancer patients (n=21 and 54 patients respectively, log rank test). (h and i) RT-qPCR detection of *MAYA* and CTGF expression level in MCF-7 cells transfected with the indicated siRNAs that grown under spare or confluent culture conditions (h) or followed by lysophosphatidic acid (LPA) treatment (1 μM, 2 hrs) (i). For h and i, mean ± s.e.m. were derived from n=3 independent experiments (n.s., p>0.05 and **p<0.01, two-tailed paired Student's t-test). Unprocessed original scans of all blots/gels with size marker are shown in Supplementary Fig. 9.

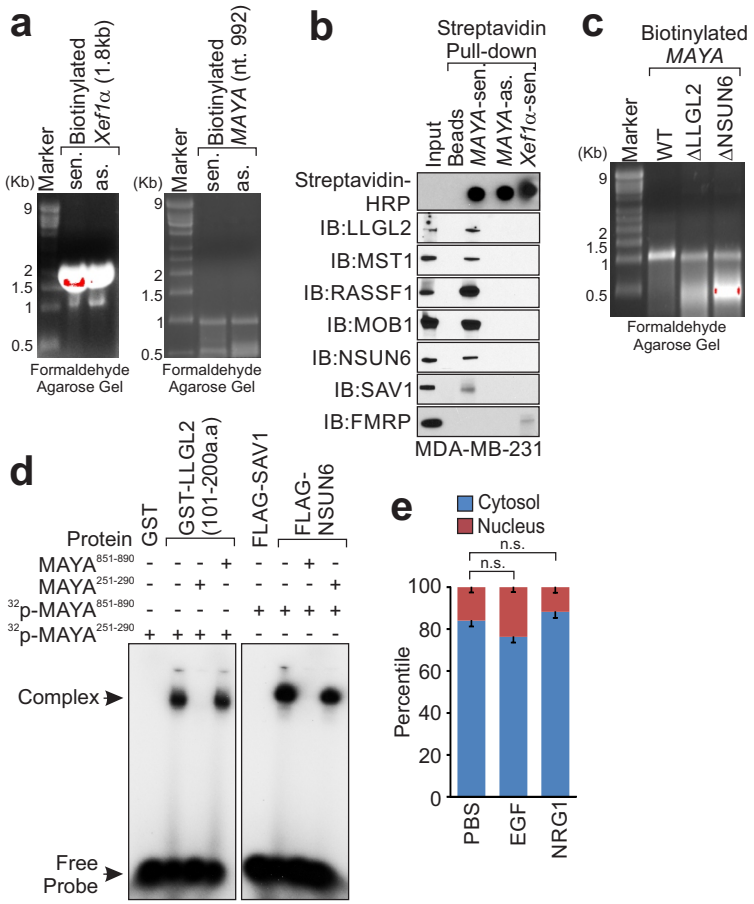

Supplementary Figure 5 Characterization of *MAYA*-LLGL2 and *MAYA*-NSUN6 interactions. (a) Electrophoresis of *in vitro* transcribed *Xef1α* (left) or *MAYA* (right) sense (sen.) and anti-sense (as.) transcripts. (b) Streptavidin RNA pull-down assay, followed by IB detection of indicated proteins, using *MAYA* sense (sen.), anti-sense (as.) and *Xef1α* sense RNA. The presence of RNA transcripts was detected by streptavidin-HRP using dot-blot assay. (c) Electrophoresis of in vitro transcribed full-length *MAYA* or truncated transcripts. (d) RNA REMSA assay was performed using recombinant GST-tagged LLGL2 (aa. 101-200) or FLAG-tagged NSUN6 in the presence of ^{32}P-labeled or cold *MAYA* RNA probes (nt. 251-290 and nt. 851-890), respectively. (e) Cell fractionation followed by RT-qPCR detecting relative *MAYA* expression in MDA-MB-231 cells with indicated stimuli (mean ± s.e.m. were derived from n=3 independent experiments, n.s., p>0.05, two-tailed paired Student's t-test). Unprocessed original scans of all blots/gels with size marker are shown in Supplementary Fig. 9. An unprocessed original scans of EMSA image for d is also shown in Supplementary Fig. 9.

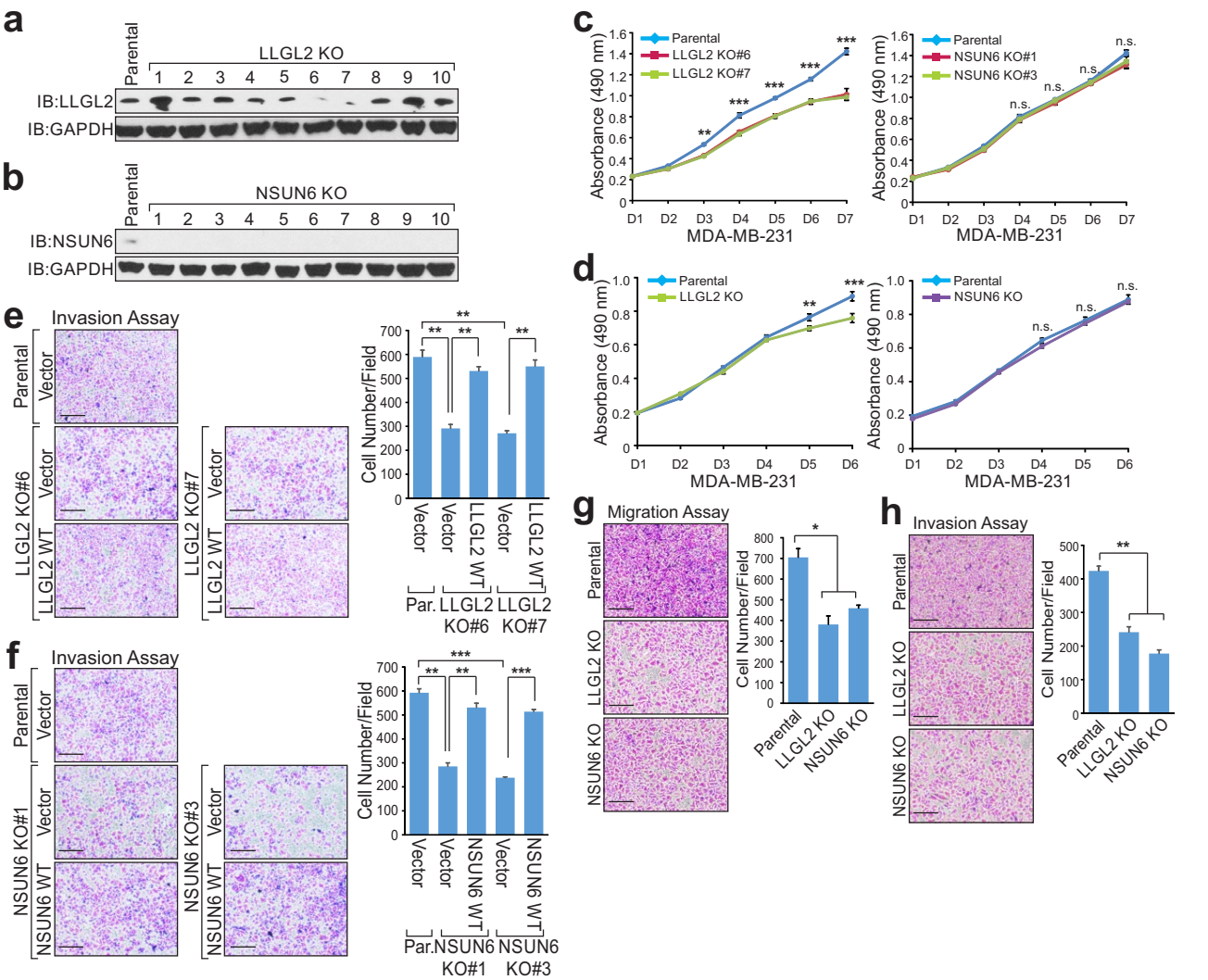

Supplementary Figure 6 Examination of the role of LLGL2 and NSUN6 in breast cancer cells. (a and b) IB detection of the indicated proteins in LLGL2 KO (a) and NSUN6 KO (b) MDA-MB-231 cells. (c and d) Cell proliferation assay of individual (c) and pooled (d) clones of LLGL2 KO (left panels) and NSUN6 KO (right panels) MDA-MB-231 cells. (e and f) Cell invasion assay of individual clones of LLGL2 KO (e) and NSUN6 KO (f) MDA-MB-231 cells with overexpression of indicated plasmid (left, scale bars: 200 μm; right, quantification). (g and h) Cell migration (g) and invasion (h) assay of pooled clones of LLGL2 KO and NSUN6 KO MDA-MB-231 cells (left, scale bars: 200 μm; right, quantification). For c-h, mean ± s.e.m. were derived from n=3 independent experiments (n.s., p>0.05, *p<0.05, **p<0.01 and ***p<0.001, two-tailed paired Student's t-test). Unprocessed original scans of all blots with size marker are shown in Supplementary Fig. 9. Source data for e-h are in Supplementary Table 8.

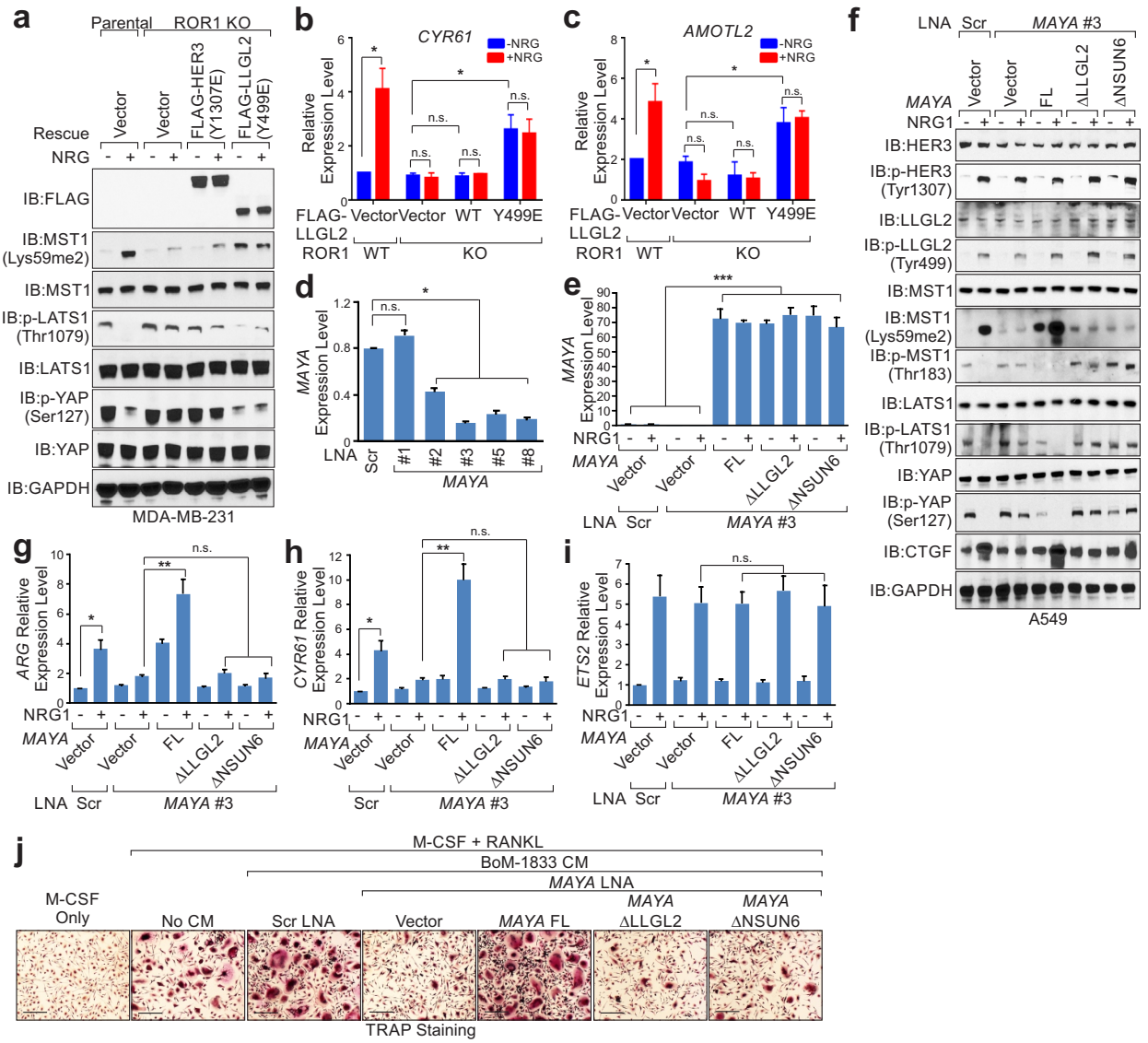

Supplementary Figure 7 *MAYA* is required for NRG1-triggered ROR1-HER3-MST1-YAP signaling axis. (a) IP and IB detection of indicated proteins in ROR1 KO MDA-MB-231cells transfected with indicated expression vectors followed by NRG1 stimulation. (b and c) RT-qPCR detection of indicated genes in ROR1 KO cells transfected with indicated expression vectors followed by NRG1 stimulation. (d) *MAYA* expression level in MDA-MB-231 cells transfected with indicated individual LNAs targeting *MAYA*. (e) RT-qPCR detection of *MAYA* expression in MDA-MB-231 cells transfected with LNAs against *MAYA* followed by overexpression of indicated plasmids and NRG1 treatment. (f) IB detection of indicated proteins in A549 cells transfected with LNAs against MAYA followed by overexpression of indicated plasmids and NRG1 treatment. (g-i) RT-qPCR detection of indicated gene expression in MDA-MB-231 cells transfected with LNAs against *MAYA* followed by overexpression of indicated plasmids and NRG1 treatment (100 ng ml^{-1} for 1 hr). (j) Osteoclast differentiation in the presence of M-CSF only, M-CSF+RANKL, or combined M-CSF+RANKL and CM from scramble (Scr) or *MAYA* LNA-transfected BoM-1833 cells rescued with indicated plasmids (scale bars: 200 μm). For b-e and g-i, mean ± s.e.m. were derived from n=3 independent experiments (n.s., p>0.05, *p<0.05, **p<0.01 and ***p<0.001, two-tailed paired Student's t-test). Unprocessed original scans of all blots with size marker are shown in Supplementary Fig. 9. Statistics source data for j are in Supplementary Table 8.

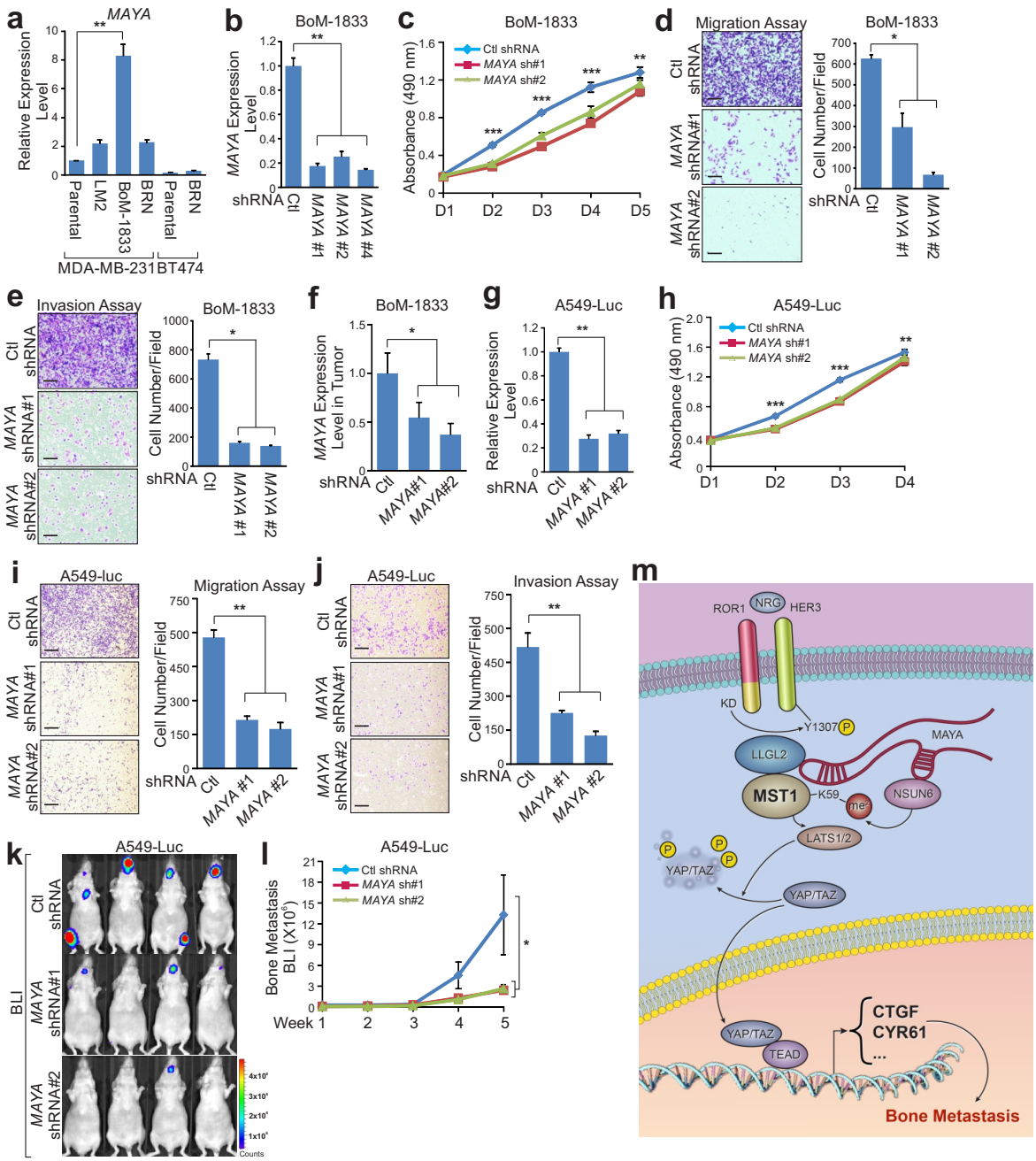

Supplementary Figure 8 Targeting *MAYA* inhibits the migration of lung cancer cells *in vitro* and tumor bone metastasis *in vivo*. (a) RT-qPCR detection of *MAYA* expression level in a panel of breast cancer cell lines. (b) RT-qPCR detection of *MAYA* expression level in BoM-1833 cells harboring indicated shRNAs. (c) Cell proliferation assay of BoM-1833 cells harboring indicated shRNAs. (d and e) Cell migration (d) and invasion (e) assays using BoM-1833 cells harboring indicated shRNAs (left, scale bars: 200 μm; right, quantification). (f) RT-qPCR detection of *MAYA* expression level in bone tumors of nude mice inoculated with BoM-1833 cells harboring indicated shRNAs. (g) RT-qPCR detection of *MAYA* expression level in A549-Luc cells harboring indicated shRNAs. (h) Cell proliferation assay of A549-Luc cells harboring indicated shRNAs. (i and j) Cell migration (i) and invasion (j) assays using A549-Luc cells harboring indicated shRNAs (left, scale bars: 200 μm; right, quantification). (k and l) Representative BLI images (k) and bone colonization (l) of nude mice with intra-cardiac injection of A549-Luc cells harboring indicated shRNAs (n=5 mice *per* group). (m) Graphic illustration of the functional role of NRG1-HER3 triggered, *MAYA*-mediated Hippo signaling suppression and YAP targets activation for promoting bone metastasis. For a-j and l, mean ± s.e.m. were derived from n=3 independent experiments (*p<0.05, **p<0.01 and ***p<0.001, two-tailed paired Student's t-test). Statistics source data for d, e, i, j and k-l are in Supplementary Table 8.

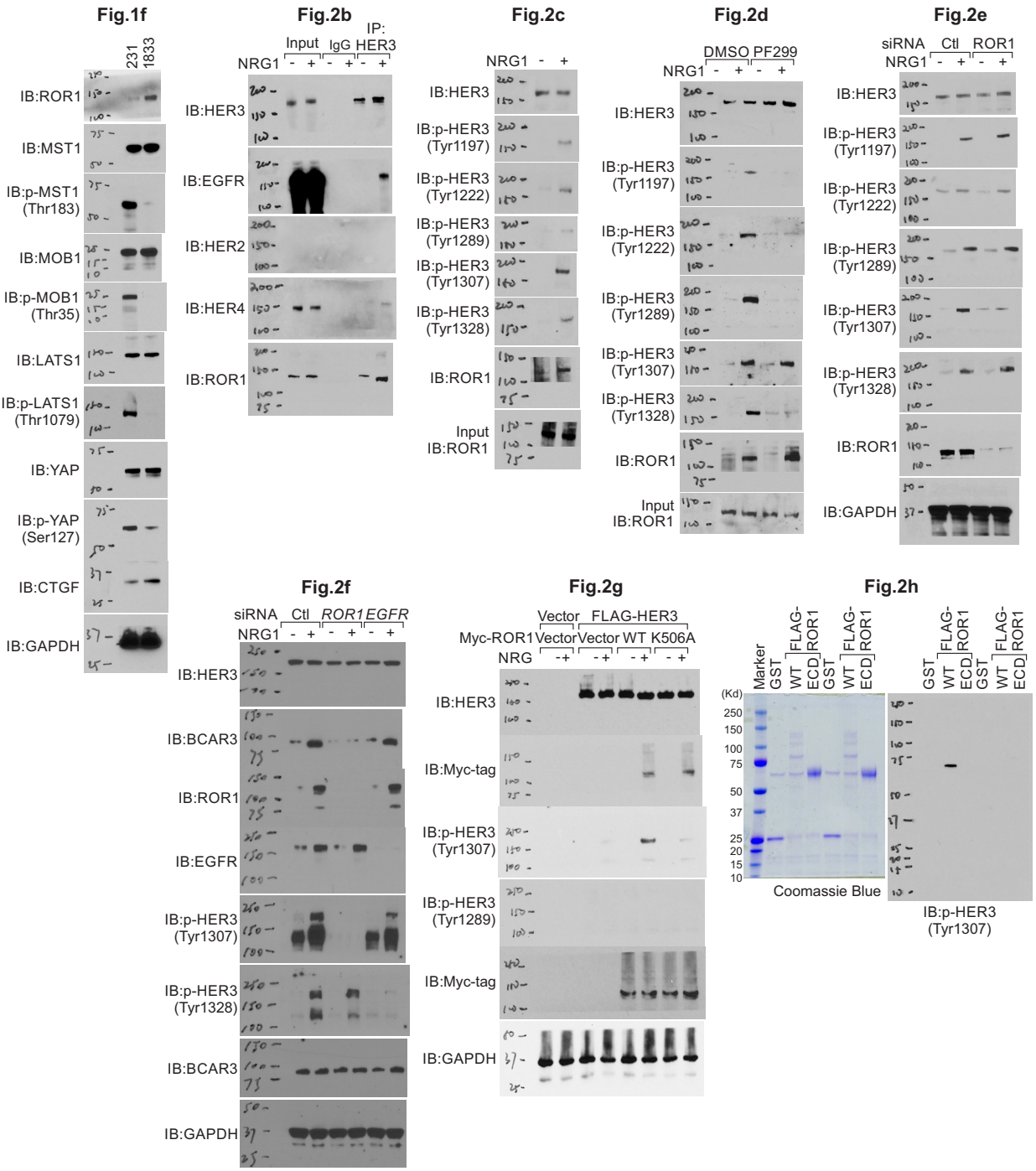

Supplementary Figure 9 Uncropped images of immunoblots and nucleic acid electrophoresis. Uncropped scan of images for all immunoblotting and nucleic acid electrophoresis experiments are shown.

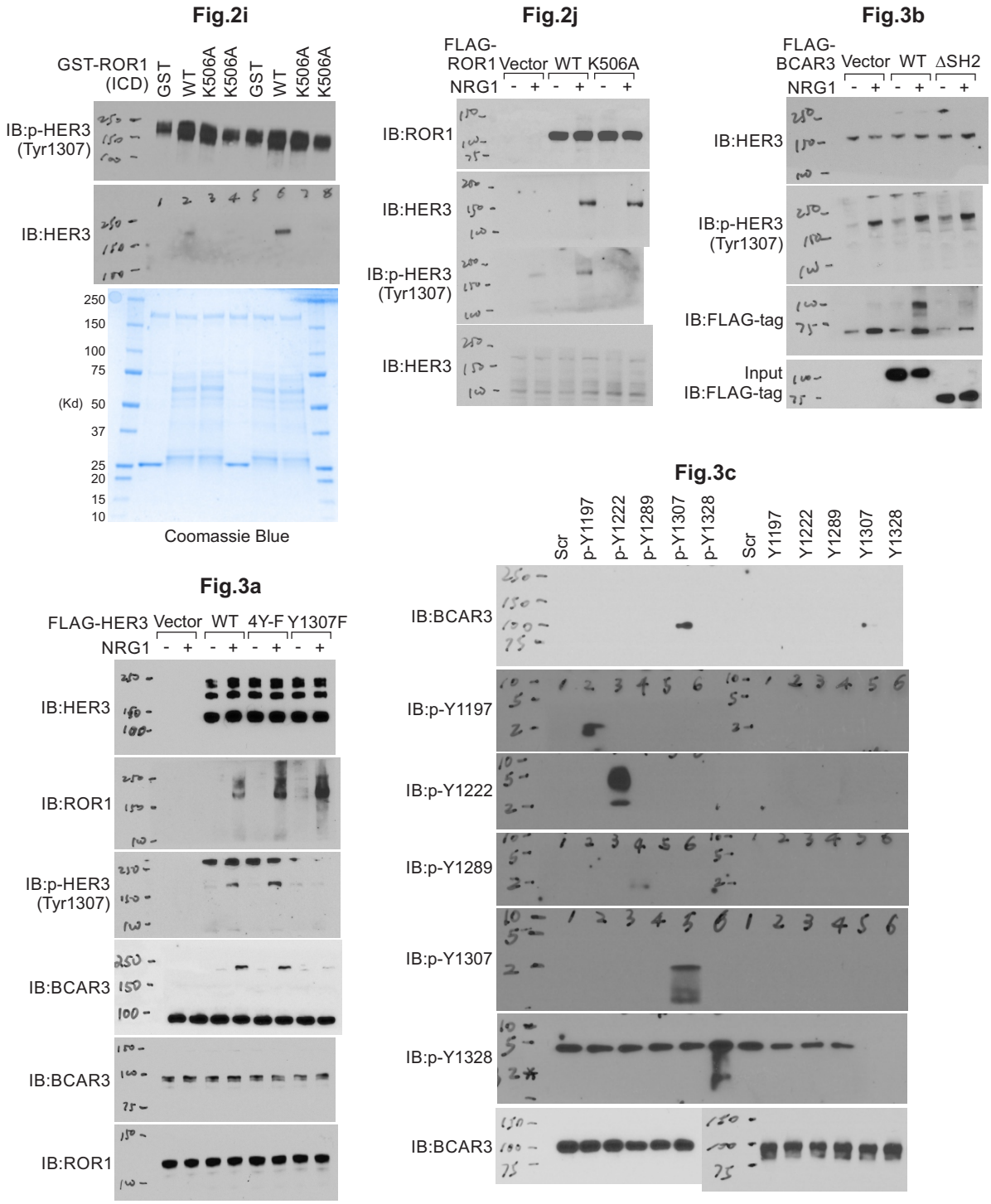

Supplementary Figure 9 Continued

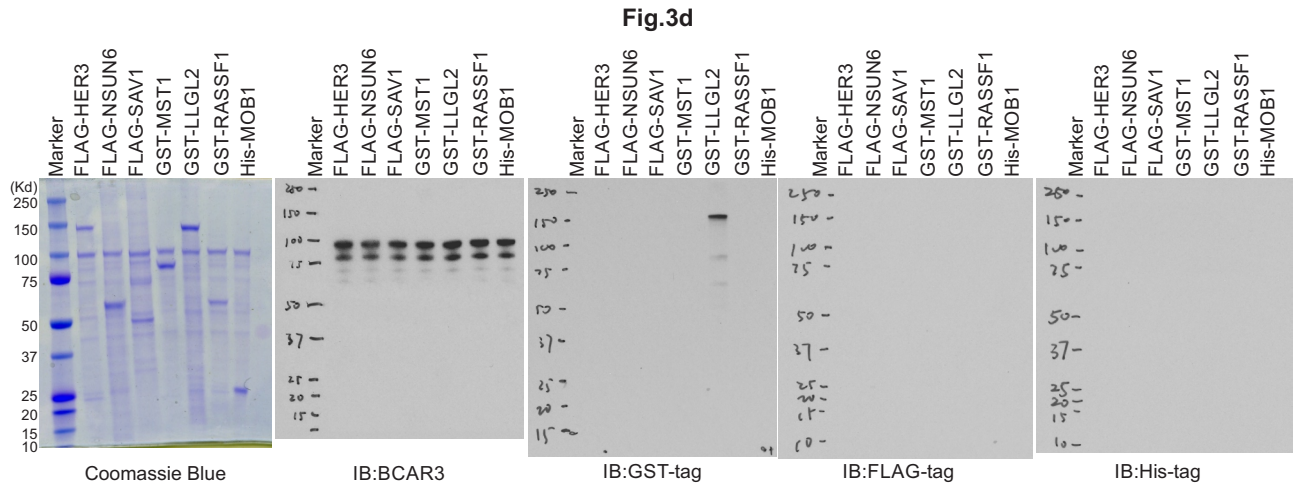

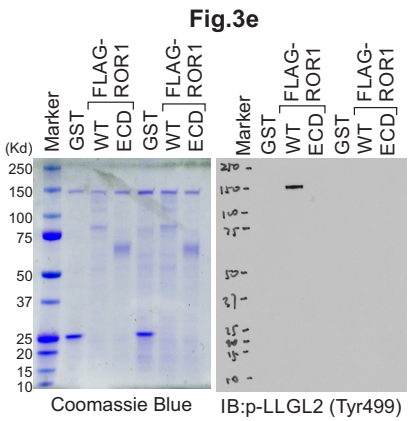

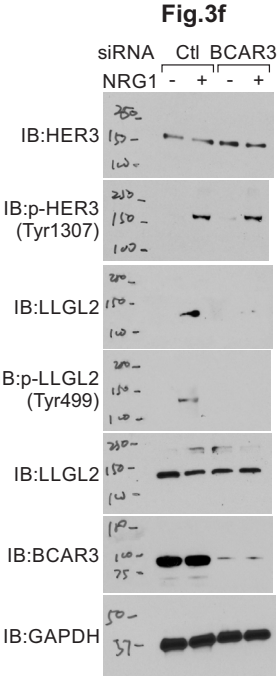

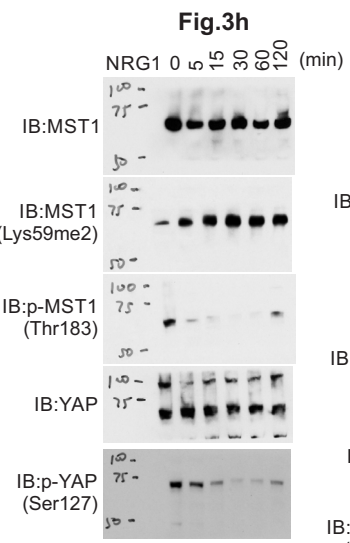

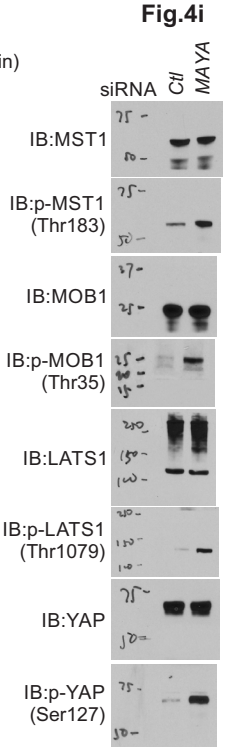

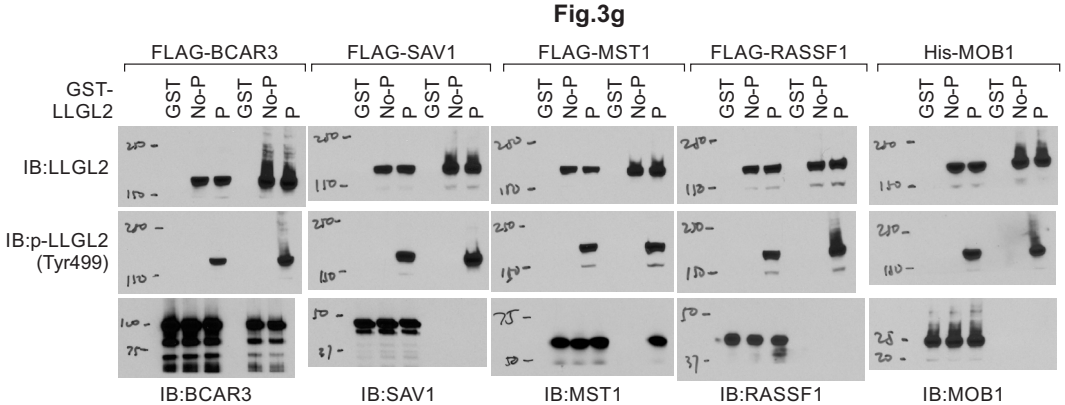

Supplementary Figure 9 Continued

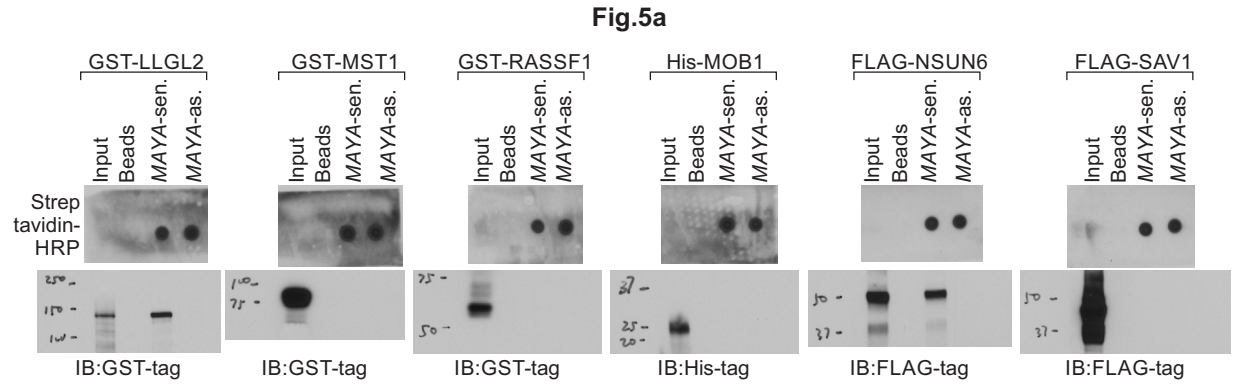

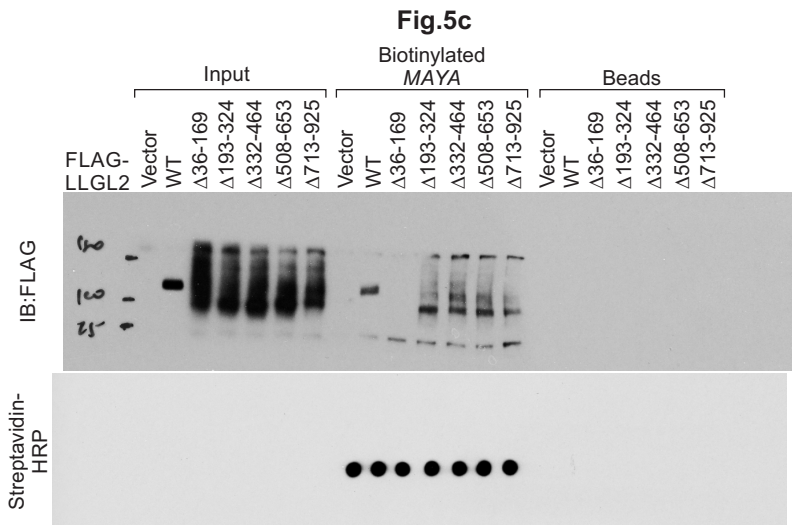

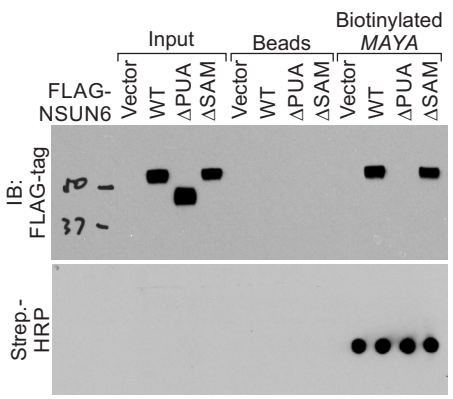

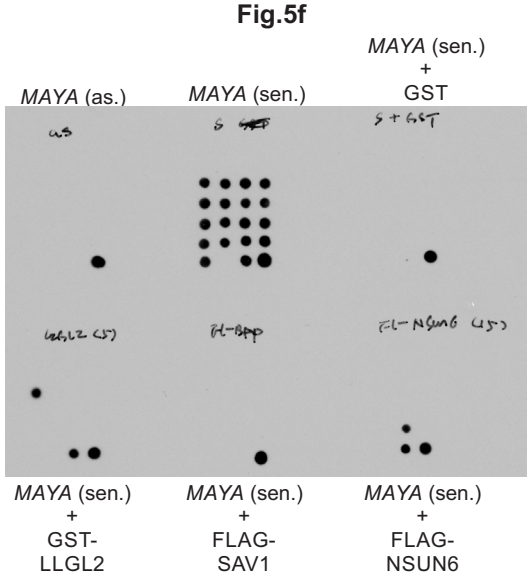

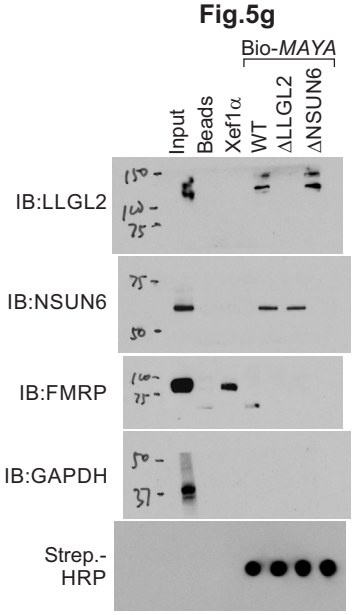

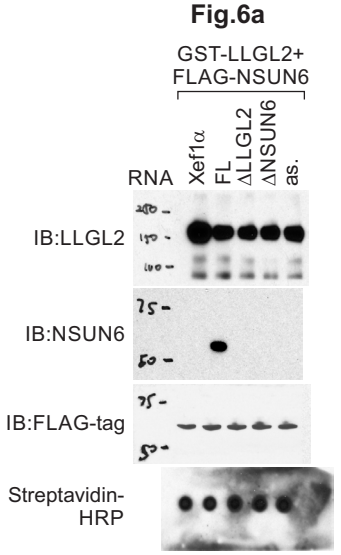

Supplementary Figure 9 Continued

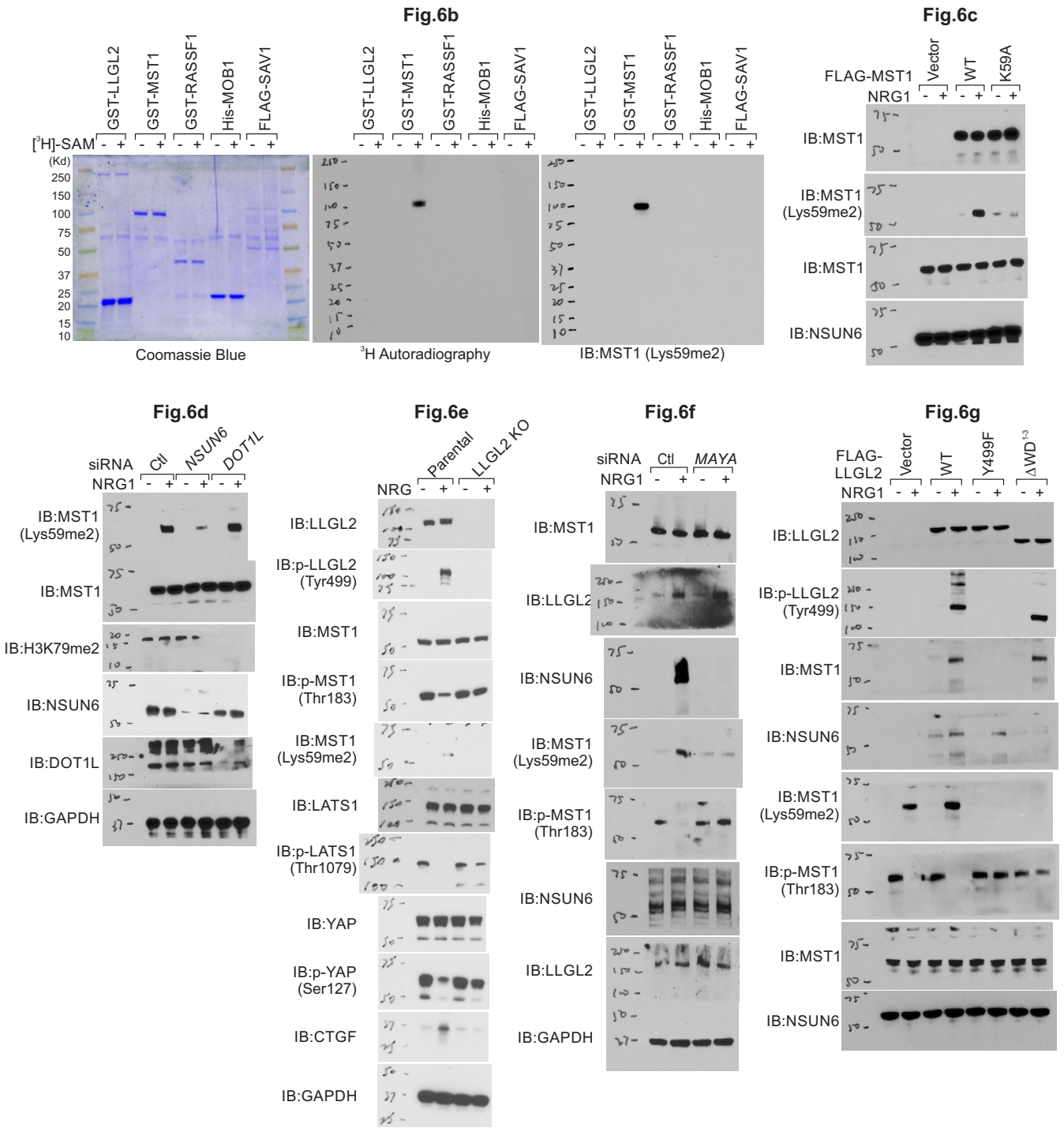

Supplementary Figure 9 Continued

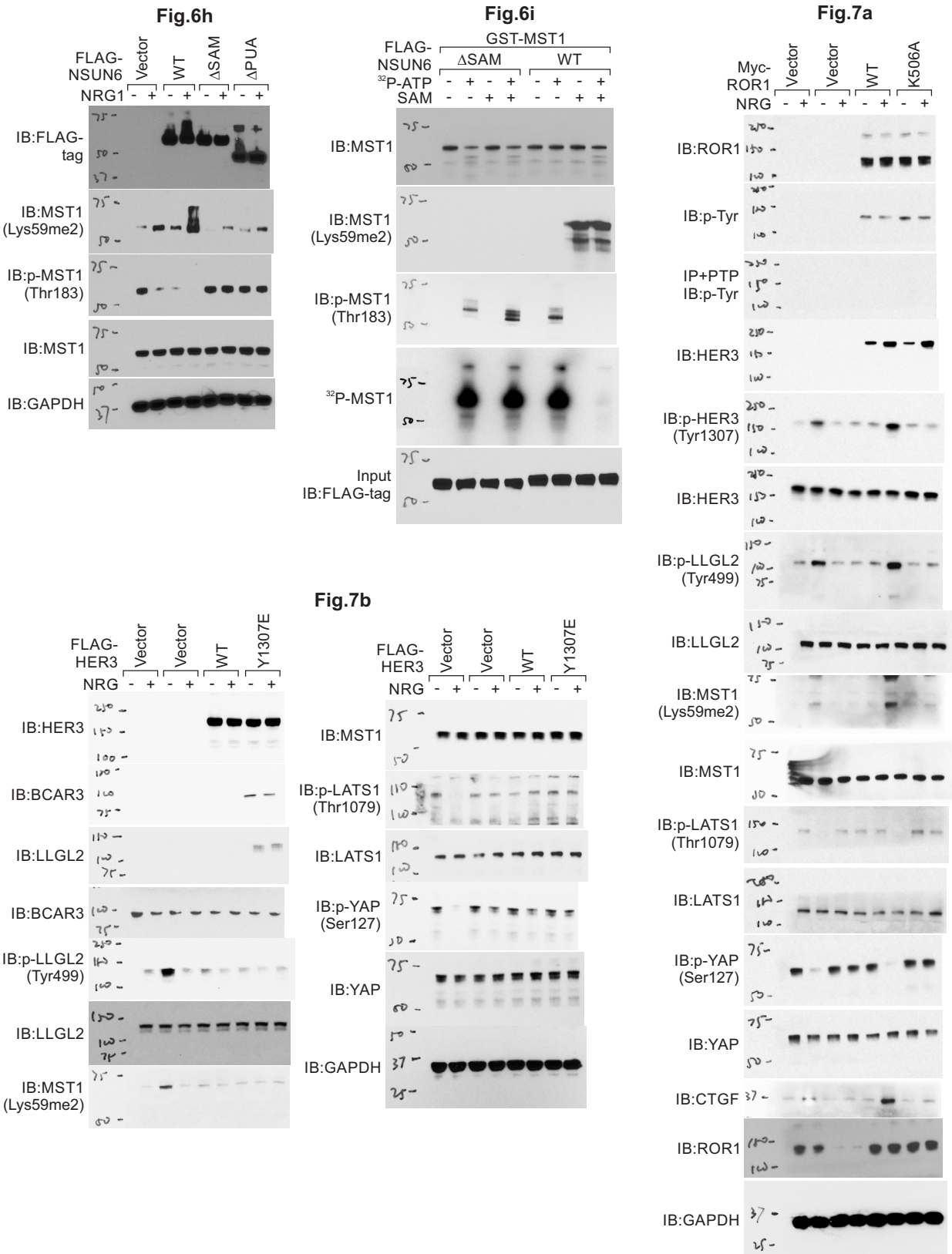

Supplementary Figure 9 Continued

Fig.7c

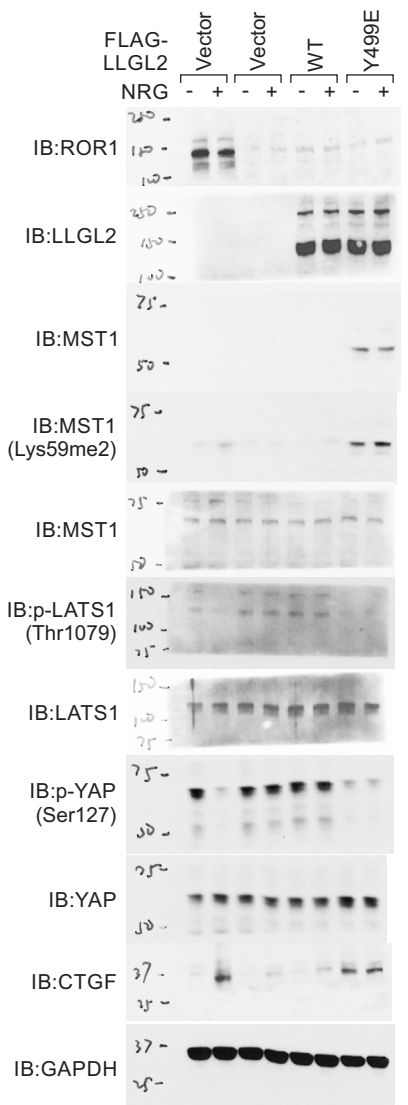

Fig.7e

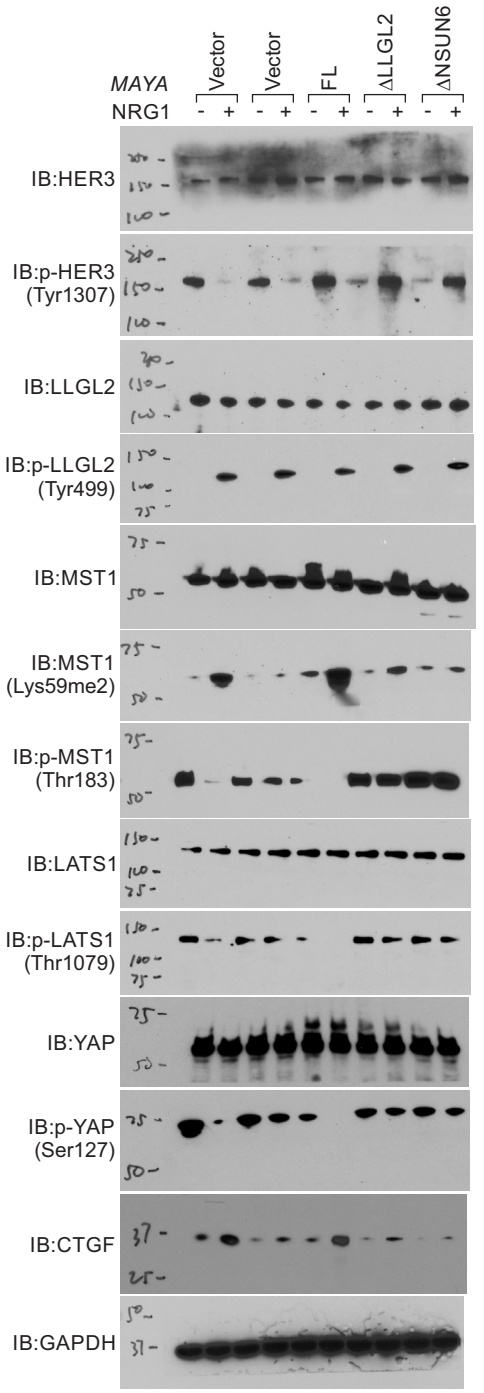

Fig.8a

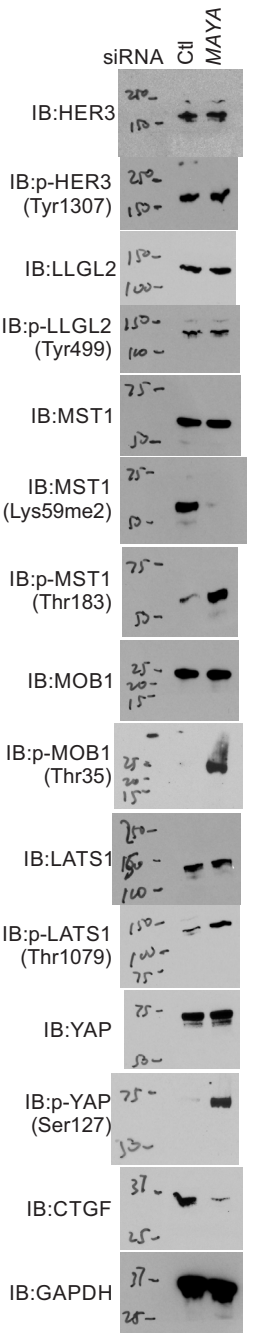

Supplementary Figure 9 Continued

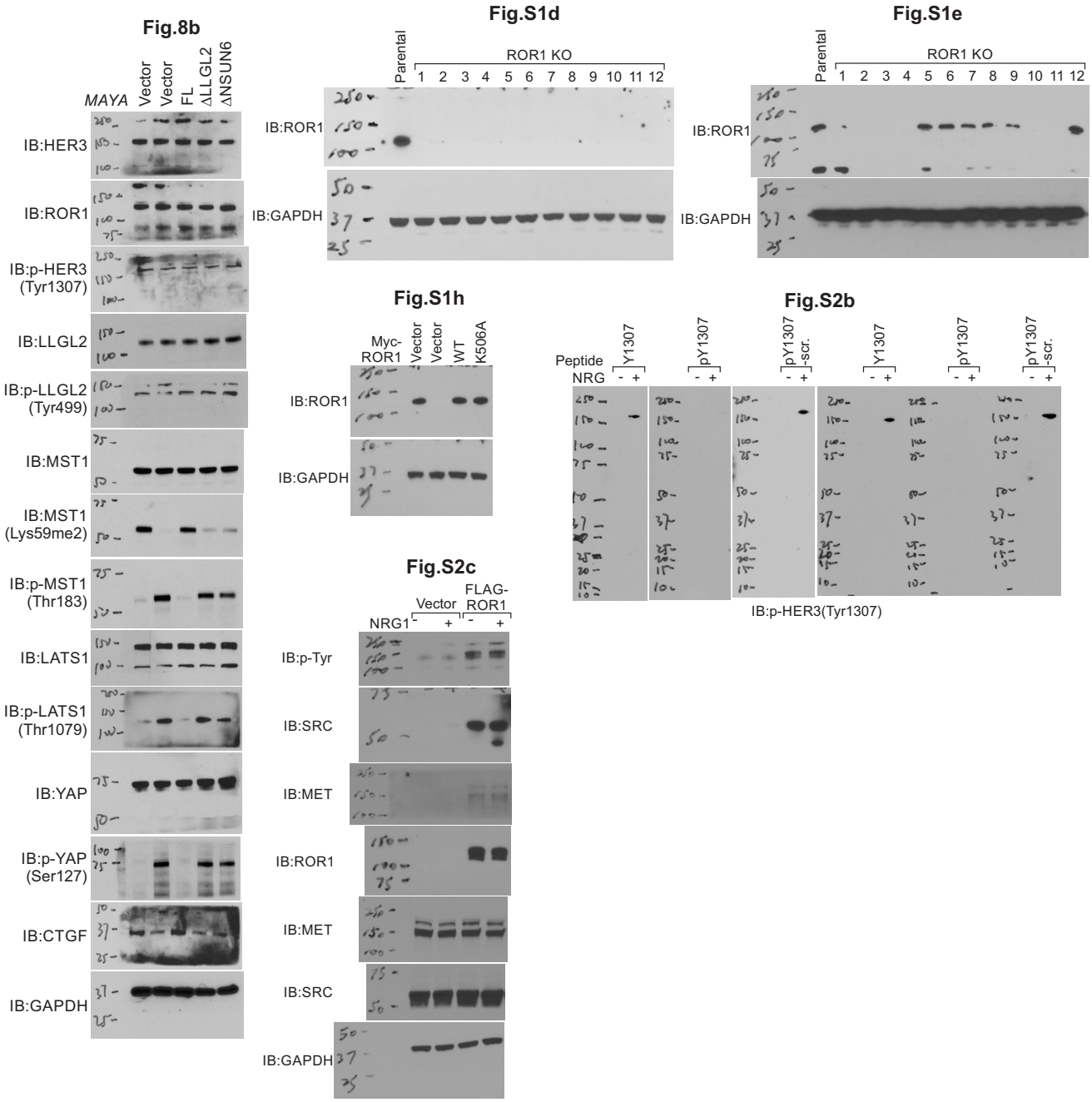

Supplementary Figure 9 Continued

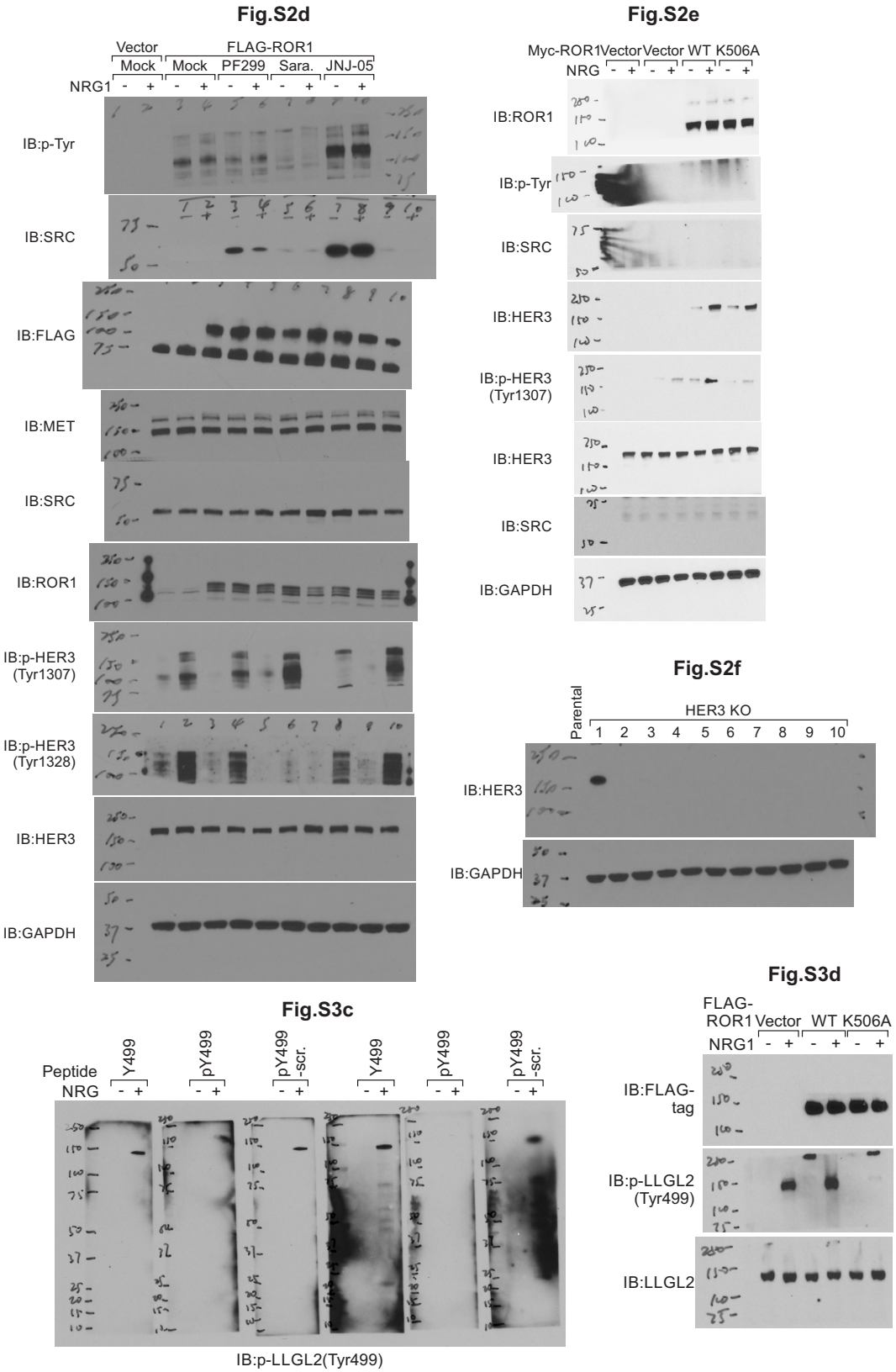

Supplementary Figure 9 Continued

Fig.S3f

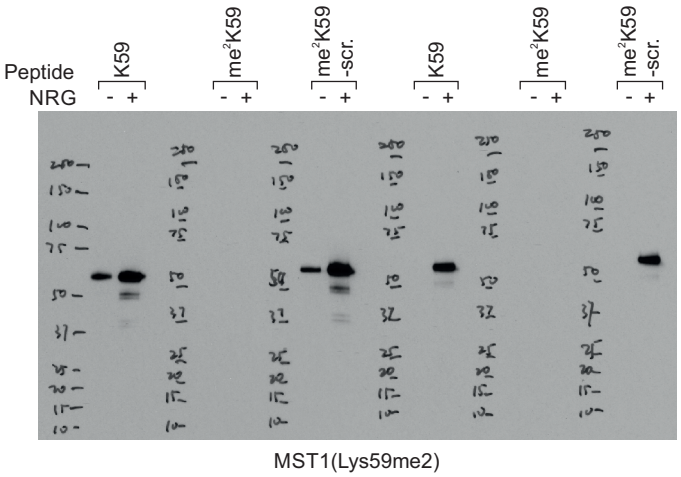

Fig.S3g

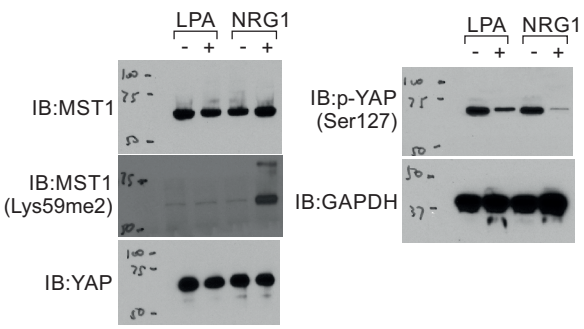

Fig.S4b

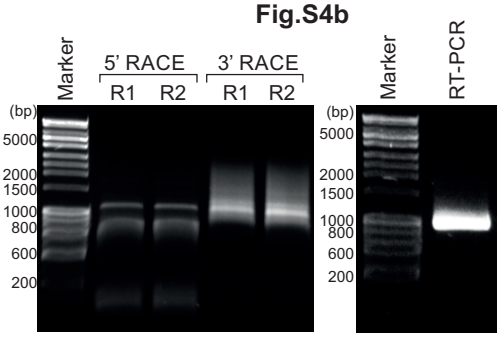

Fig.S4c

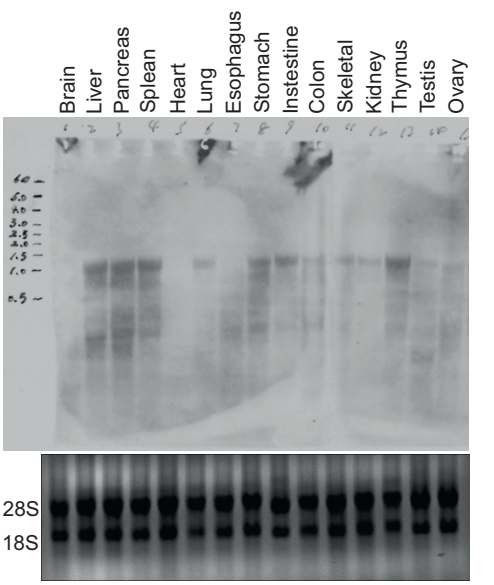

(Gel image of RNA purity and integrity for pre-made Northern blot cat# HN-MT-1, obtained from Zyagen)

Fig.S4d

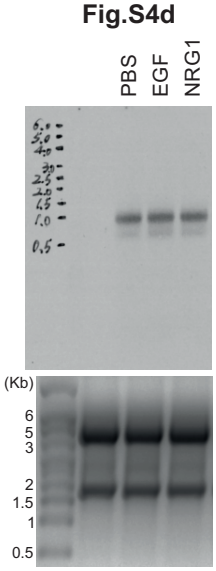

Fig.S5a

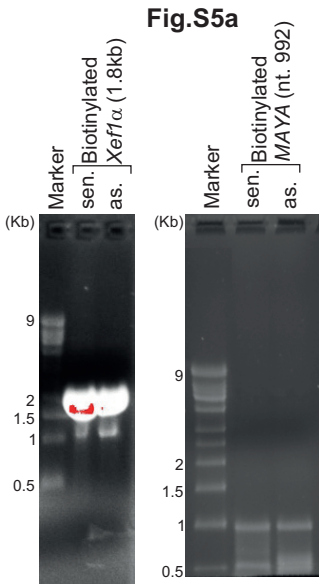

Fig.S5b

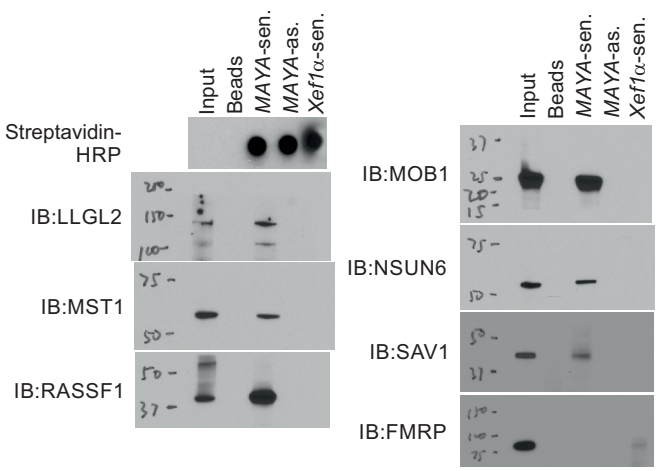

Supplementary Figure 9 Continued

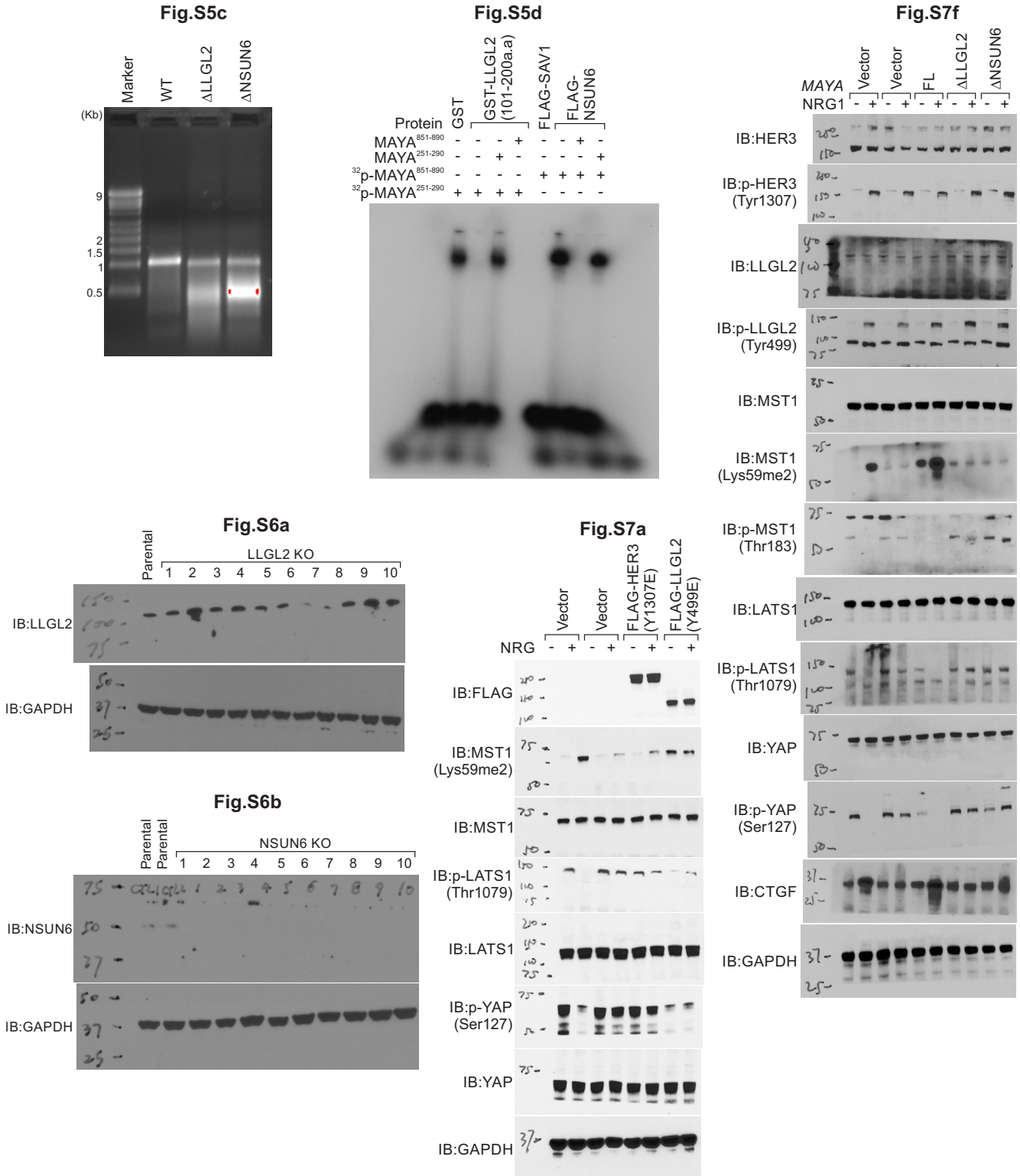

Supplementary Figure 9 Continued

Supplementary Table Legends

Supplementary Table 1 Clinicopathological parameters of tissue microarrays used in this study. Bre170Sur-01: Breast cancer, 170 cases. 160 cases have tumor, 1 core/case, 10 cases have normal adjacent tissue, 1 core/case, with survival information; T6235086-5: Breast Human Tumor Frozen Tissue Microarray, 37 frozen breast tumor and 3 frozen normal breast tissue specimens; BRF404b: Frozen breast cancer tissue array with adjacent breast tissue as control, 20 cases/ 40 cores, with IHC results of HER2, ER, PR; LugS150Sur-01: Lung squamous cell carcinoma (75 cases), tumor (1 core/case) and matched normal adjacent tissue (1 core/case), with survival information; LC2161: Lung cancer tissue array, including TNM and pathology grade, 216 cases/216 cores; MC1801: Multiple-organ tumor tissue array, including TNM, clinical stage and pathology grade, 180 cases/180 cores; HBre-Duc150Sur-01: Breast carcinoma, 150 cases, 1 core/case, with Clinical stage I, II, III and Survival data followed up for 9-12 years; BR243m: Breast cancer tissue array with matched adjacent breast tissue as control, including TNM, clinical stage and pathology grade, 6 cases/ 24 cores; Hlug-Ade150Sur-01: Lung adenocarcinoma tissue array, 75 cases of tumor and matched normal adjacent tissue (NAT), 1 core/case with TNM and survival information; Yixin Bre-01: Frozen breast cancer tissue array with adjacent breast tissue as control, 20 cases/ 40 cores, with IHC results of HER2, ER, PR; TMA-009: Breast cancer tissue array including TNM, clinical stage and pathology information, 45 cases/ 45 cores; T6235700-5: Frozen Tumor and Normal Tissue Array, tumor and normal tissues from 14 different human organs.

Supplementary Table 2 LC-MS/MS protein identification results for ROR1 pull-down experiments. Complete mass spectrometry results for ROR1 associated proteins pulled down from MDA-MB-231 cell lysates. This table has two tabs, listing the number of unique and shared peptides identified for IgG and ROR1.

Supplementary Table 3 LC-MS/MS protein identification results for LLGL2 pull-down experiments. Complete mass spectrometry results for LLGL2 associated proteins pulled down from MDA-MB-231 cell lysates. This table has two tabs, listing the number of unique and shared peptides identified for IgG and LLGL2.

Supplementary Table 4 Top 40 Hits from the human Lincode siRNA library screening in MCF7-Hippo/TEAD reporter cell line. The Human Lincode siRNA Library were transfected into MCF7-Hippo/TEAD reporter cell line and the luciferase activity and protein concentrations were measured after 72 hours. Raw luciferase signal intensities were first normalized by protein concentrations, and normalized luciferase signal intensities were further divided by luciferase signal intensities from control siRNA samples to obtain fold change, which was shown as log scale. The top 40 hits (≥ 8 fold changes, *MAYA* siRNA *vs.* Ctl siRNA) were shown.

Supplementary Table 5 LC-MS/MS protein identification results for biotinylated *MAYA* RNA pull-down experiments. Complete mass spectrometry results for Biotinylated *MAYA* associated proteins pulled down from MDA-MB-231 cell lysates. This table has three tabs, listing the number of unique and shared peptides identified for monoavidin magnetic beads, sense and anti-sense *MAYA* RNAs.

Supplementary Table 6 List of antibodies used in this study. Commercially available/custom generated antibodies and their catalogue number, clone number and usage are listed.

Supplementary Table 7 List oligonucleotides used in this study. The sequence for all shRNAs/LNAs, primers for PCR/RT-qPCR, probes for Northern blot/ EMSA/RNA FISH are provided in this table.

Supplementary Table 8 Statistics source data. Raw data of the statistical analysis for experiments with representative images are provided.